MATERIALS SCIENCE

Construction of solid-liquid fluorine transport channel to enable highly reversible conversion cathodes

Keyi Chen[1,2,3], Meng Lei[1,3], Zhenguo Yao[1,2], Yongjian Zheng[1,2,3], Jiulin Hu[1,2,3], Chuanzhong Lai[1,2,3], Chilin Li[1,2,3]*

Conversion-type iron fluoride is a promising alternative cathode to intercalation oxides because of its higher energy density. However, its intrinsic solid-solid conversion is sluggish during repeated splitting and rebonding of metal-fluorine moieties. Here, we propose a solid-liquid conversion mechanism to activate the fluorine transport kinetics of iron oxyfluorides enabled by fluoride anion receptor of tris(pentafluorophenyl)borane (TPFPB). TPFPB promotes the dissociation of inert lithium fluoride and provides a facile fluorine transport channel at multiphase interfaces via the formation of solvated F^- intermediate therein. The construction of solid-liquid channel with fluorinated cathode electrolyte interface is the key for the achievement of $FeO_{0.3}F_{1.7}$ and $FeO_{0.7}F_{1.3}$ in terms of sustaining conversion reaction (with an energy efficiency approaching 80%) and high-rate performance (with reversible capacity of 320 mAh/g at 2 A/g). The cathode energy densities can reach 1100 Wh/kg for $FeO_{0.3}F_{1.7}$ and 700 Wh/kg for $FeO_{0.7}F_{1.3}$ under the power densities of 220 and 4300 W/kg, respectively.

INTRODUCTION

With the ever-increasing demand on high energy density, lithium-ion batteries are not satisfactory as next-generation energy storage technology for large-scale application of powerful electromobility systems such as electric vehicles and all-electric aircraft (*1*). Therefore, lithium metal batteries based on Li metal anode coupled with conversion-type cathode have emerged at the needed moment, and they are usually characterized by high operational voltages and high specific capacities (*2*). Beyond the limitation of intercalation chemistry with single-electron transfer, conversion reaction compounds could achieve multiple-electron transfer per active center, and accordingly, have promising opportunities for high–energy density storage (*3*). Although the typical Li—O_2 and Li—S batteries have attracted extensive attention because of their high theoretical gravimetric capacities, the reaction zone confinement is still a serious problem for molecule-type cathodes. It would trigger the loss of active species and a series of detrimental side reactions with electrolyte or metal anode (*4*). Furthermore, the molecule-type cathodes with loose distribution would degrade the volume energy density of conversion batteries. Condensed metal fluorides (MF_x) can serve as another type of conversion cathodes in terms of the uplifted operational voltages due to the highest electronegativity of F element (*5*). Combined with the high specific capacity via the reaction process of $MF_x + xLi^+ + xe^- = M + xLiF$, fluorides could deliver considerable energy densities, which can compete with those of S/Li_2S or O_2/Li_2O_2 cathodes and even exceed them especially when referring to volumetric performance (*2*). The built-in conductive network and good confinement effect in fluoride can minimize the use of inactive conductive additive without serious degradation of interfacial electric contact and reversible multiphase transition (*6*). Among them, environmentally friendly and cheap iron trifluoride (FeF_3) is considered as a promising cathode candidate, which can offer an extremely high energy density of 1947 Wh/kg (based on a theoretical capacity of 712 mAh/g with a thermodynamic potential of ~2.73 V) via three-electron transfer (*2*). However, the sluggish kinetics would lower the practical voltage and capacity during multiphase conversion reaction with repeated splitting and rebonding of metal-fluorine (M-F) moieties as well as intrinsic low electronic conductivity induced by the high ionicity of M-F bonding (*5*, *7*).

Commercially available ReO_3-type FeF_3 with dense structure is neither electronically nor ionically conductive. It cannot be used as the desired host for highly reversible conversion reaction (*8*). Open-framework strategy is an effective solution to the kinetic activation of fluorides via the introduction of channel stuffing (e.g., K^+ and H_2O) to extend the solid solution reaction zone (*9*, *10*). Nevertheless, the optimized parent phase seems difficult to be electrochemically reconstituted once structure collapse occurs during conversion reaction. Although facile charge/mass transport is available via nano-engineering, morphology regulation, and compositing with conductive wires, the high electrochemical reversibility of iron fluorides is still a big challenge especially when involving conversion reaction (*11*, *12*). Mixed anion chemistry or defect introduction also enables an improvement in Li storage capability despite the complexification of reaction mechanism (*13*, *14*). The substitution of oxygen for fluorine in FeF_2 can generate a series of iron oxyfluorides FeO_xF_{2-x} ($0 \le x \le 1$) with identical rutile structure, which is an effective way to substantially improve the intrinsic electron conductivity (*13*). The modification brings about a partitioned evolution pathway of anion components after the sufficient Li^+ intercalation of rutile (*15*). Thus, the O-doped fluorides could achieve a better electron transfer and higher reversible capacity (beyond insertion stage) without the decomposition of host lattice (*16*, *17*). However, the kinetic problem involving multiphase reaction remains unsolved, leading to the unsatisfactory rate performance. On the other hand, the electrolyte composition would have marked impact on cell performance especially when coupling the cathodic redox behavior or anodic Li-plating/stripping behavior. The cathode electrolyte interface (CEI) derived during cycling can serve as a protective layer to hinder the dissolution of Fe-based active species and its parasitic reaction with electrolyte (*18*). Some fluorine-containing Li salts or additives can contribute

[1]State Key Laboratory of High Performance Ceramics and Superfine Microstructure, Shanghai Institute of Ceramics, Chinese Academy of Sciences, 585 He Shuo Road, Shanghai 201899, China. [2]Center of Materials Science and Optoelectronics Engineering, University of Chinese Academy of Sciences, Beijing 100049, China. [3]CAS Key Laboratory of Materials for Energy Conversion, Shanghai Institute of Ceramics, Chinese Academy of Sciences, Shanghai 201899, China.
*Corresponding author. Email: chilinli@mail.sic.ac.cn

to yield the smoother morphology of cycled lithium anode (*19*, *20*). The in situ formation of CEI triggered by highly concentrated electrolyte [e.g., with 4.6 M lithium bis(fluorosulfonyl)imide (LiFSI)] could improve the cycling stability of conversion reaction to a certain degree (*20*, *21*). However, excessive solvated salts with few free-moving solvents may unfavorably increase the electrolyte viscosity and decrease the bulk ionic mobility (*22*), which would drag on the electrochemical reaction rate of electrode and degrade its polarization performance. The liquid electrolyte–induced problems can be avoided by using quasi/all-solid-state architecture (*23*, *24*), but their inherent hurdles of sluggish bulk ion migration and solid-solid interface degradation still require to be overcome. These common modification strategies for cathode or electrolyte seem not to well address the conversion kinetics of iron-based fluorides. In particular for Li-driven fluoride conversion, heterogeneous precipitation and coverage of insulating lithium fluoride (LiF) on the whole electrode surface would impede the internal chemical reaction between active fluoride and lithium, consequently causing large voltage hysteresis and low available capacity. Hence, the key factors required to be taken seriously for fluoride activation are rational spatial distribution of multiple phases and great activation of inert LiF.

In this work, we design a solid-liquid "fluorine channel" enabled by an anion receptor of tris(pentafluorophenyl)borane (TPFPB) additive in ether-based electrolyte to activate the highly reversible conversion reaction of oxyfluorides. TPFPB molecule as F^- receptor is able to dissociate inactive LiF and form a solvated F^- intermediate $[TPFPB\text{-}F]^-$ at multiphase interface (*25*), which could provide a facile F-transport channel between LiF and Fe species by bypassing the tough solid-solid conversion. Two kinds of iron (oxy)fluoride composites with different oxygen contents (denoted as $FeO_{0.3}F_{1.7}$ and $FeO_{0.7}F_{1.3}$) were synthesized by thermal-induced self–oxygen penetration of the hydrated iron fluoride. The O doping in fluoride regulates the phase evolution pathway and introduces a stable second-generation parent phase of rock salt in the confined voltage region for conversion reaction. The construction of solid-liquid channel with the electrolyte-derivative fluorinated CEI layer promotes facile round-trip F-transport along with reversible Li insertion/extraction in oxyfluoride cathodes. As a result, both $FeO_{0.3}F_{1.7}$ and $FeO_{0.7}F_{1.3}$ cathodes achieve sustaining conversion reactions (with energy efficiency approaching 80%) and high-rate performance (with highly reversible capacities of 271 and 320 mAh/g at 2 A/g, respectively). This proposed F-activation strategy by solid-liquid conversion mechanism may be applicable for other metal fluoride conversion systems as well.

RESULTS

Physical characterization of iron oxyfluorides

The x-ray diffraction (XRD) patterns (fig. S1) are used to investigate the annealing time-dependent evolution of the crystal structure of hydrated iron fluoride (α-$FeF_3{\cdot}3H_2O$), which is precipitated from ionic liquid (IL) ambience (*26*). It reveals that the annealed fluorides have the dominant phase of tetragonal rutile structure similar to FeF_2 and FeOF with unit cell parameters between them, indicating a phase transformation of fluoride precursor at the raised temperature up to 300°C (*27*). Here, the solid solution form of FeO_xF_{2-x} ($0 \le x \le 1$) in FeF_2—FeOF system derives from both the thermodynamically favorable processes of Fe^{3+} reduction (by surrounding carbon/IL) and oxygen self-doping [via sequential hydroxylation/dehydroxylation between alternating $[FeF_2(H_2O)_4]$ and $[FeF_6]$ octahedra in $FeF_3{\cdot}3H_2O$ with the release of HF and H_2O; Fig. 1A] (*14*, *28*). For the sample annealed for 2 hours, the newly emerging diffraction peaks are mainly indexed to a FeO_xF_{2-x} phase with low oxygen content (analogous to the FeF_2 structure). The minor hexagonal tungsten bronze (HTB)-structured $FeF_3{\cdot}0.33H_2O$ is a probable intermediate phase during thermally induced transformation (*14*). After a longer heat treatment, the characteristic FeO_xF_{2-x} peaks corresponding to (101), (111), and (211) planes experience an evident shift toward higher 2θ degrees, suggesting a lattice shrinkage along with the deeper O doping and a structure evolution close to FeOF (*13*). In the meantime, the minor phase of HTB-$FeF_3{\cdot}0.33H_2O$ is full dehydrated and transformed into trigonal FeF_3. The sharper peaks also indicate improved crystallinity and grain growth during longer annealing. To determine the oxygen content x in FeO_xF_{2-x} and molar ratio of each component, the Rietveld refinements on XRD patterns were conducted (Fig. 1, B and C). The refined dominant phases in both the samples are $FeO_{0.32}F_{1.68}$ and $FeO_{0.77}F_{1.23}$ with c-lattices of 3.229 and 3.104 Å, respectively (fig. S1E). Similar a-dimension parameters of tetragonal cell account for the negligible displacement of (110) diffraction peaks. These obtained compositions and corresponding lattice parameters are in agreement with their dependency diagram of rutile-type FeO_xF_{2-x} (*29*). Here, the finally annealed products are termed as $FeO_{0.3}F_{1.7}$ and $FeO_{0.7}F_{1.3}$ according to the composition of dominant phase, respectively. The molar percentage of minor phase in $FeO_{0.3}F_{1.7}$ is estimated to be about 31.45%, whereas it is notably decreased to 14.49% after undergoing a longer O penetration reaction in $FeO_{0.7}F_{1.3}$ (table S1). Theoretical specific capacities of $FeO_{0.3}F_{1.7}$ and $FeO_{0.7}F_{1.3}$ are calculated to be 673 and 794 mAh/g on the basis of their component contents, respectively.

The scanning electron microscopy (SEM) images (Fig. 1, D and E) reveal that both the oxyfluorides display nanostructured particles wired by spherical Ketjen Black (KB carbon) grains of less than 30 nm in size. $FeO_{0.3}F_{1.7}$ particles with a size of 50 to 100 nm roughly retain the rectangle-like morphology as that of hydrated fluoride precursor precipitated at low temperature (*26*). Grain coarsening in some regions via thermal driving boundary migration could be energetically favorable for interfacial mass/charge transport (*30*). Notably, $FeO_{0.7}F_{1.3}$ grains are characterized by more disciplined morphology of octahedral geometry with a size of 100 to 200 nm. The appearance of pronounced and smooth crystallographic faces indicates the high crystallinity but with a compromise of grain growth during longer annealing process. These morphologies are in agreement with the observation from transmission electron microscopy (TEM) images (figs. S2 and S3). The diffraction rings or plots in selected area electron diffraction (SAED) patterns are basically assigned to the main phase of rutile FeO_xF_{2-x}. From the high-resolution TEM (HRTEM) images of $FeO_{0.3}F_{1.7}$, typical lattice stripes with the d-spacings of 3.35 and 2.35 Å, respectively, corresponding to (110) and (111) planes of rutile-type oxyfluoride, are clearly observable. The minor HTB-type phase is occasionally found according to the fast Fourier transform (FFT) pattern of selected lattice fringes (inset of fig. S2D). Compared with the polycrystalline diffraction rings for $FeO_{0.3}F_{1.7}$, the diffractogram of different $FeO_{0.7}F_{1.3}$ discrete crystals exhibits brighter diffraction spots with different dominant orientations of rutile-like phase, in view of its higher crystallinity (fig. S3, B and C). The typical lattice strips ascribed to (110), (101), and (111) planes of rutile phase are also discerned from HRTEM. Note that the minor phase of trigonal FeF_3 is found near the octahedron edge,

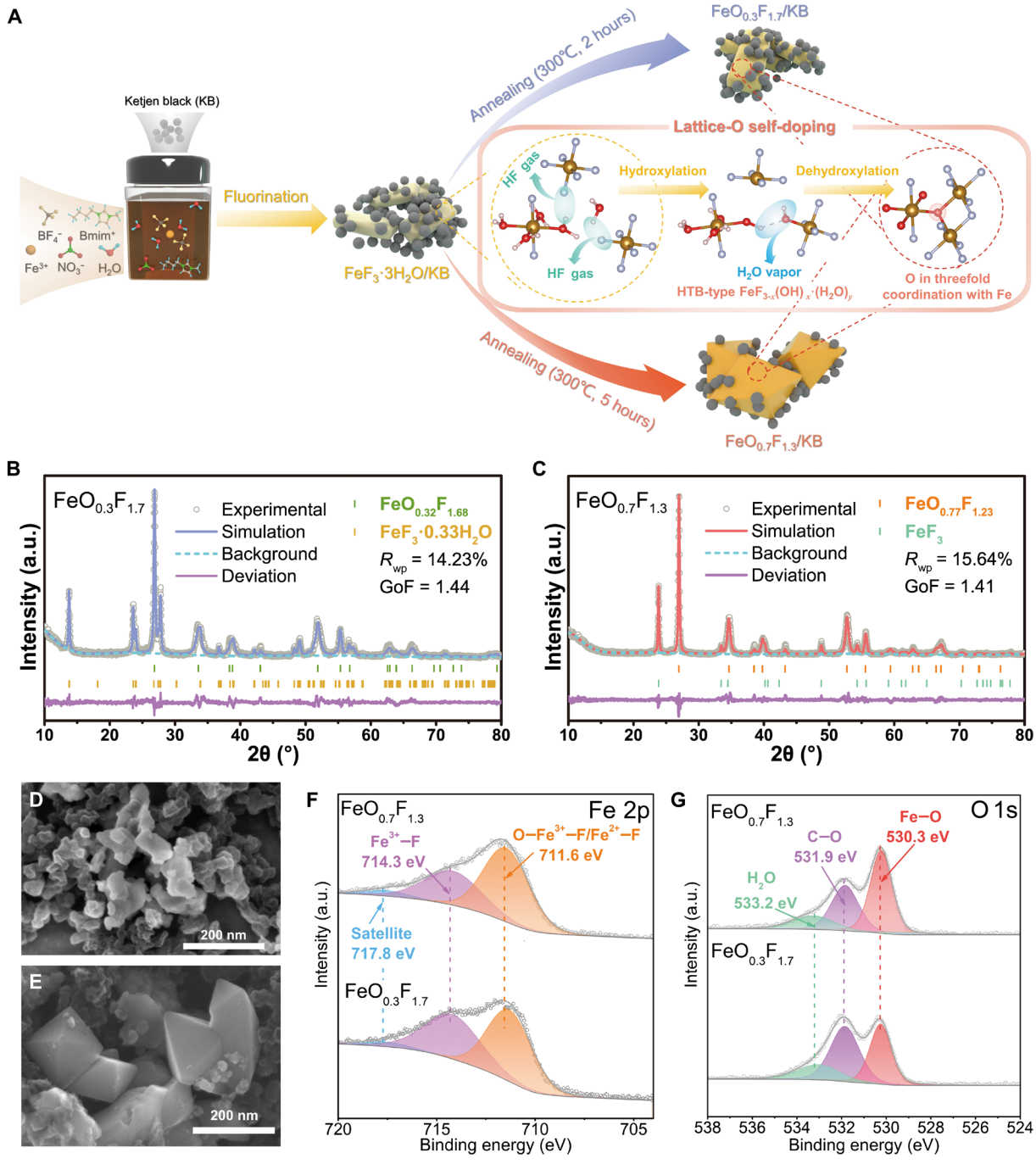

Fig. 1. Synthesis, structural, and morphological characterization of iron oxyfluorides. (**A**) Schematic illustration of synthesis process for $FeO_{0.3}F_{1.7}$ and $FeO_{0.7}F_{1.3}$ by annealing hydrated iron fluoride, as well as corresponding oxygen self-doping pathway. (**B** and **C**) XRD patterns of $FeO_{0.3}F_{1.7}$ and $FeO_{0.7}F_{1.3}$ and their Rietveld refinements. The indexes of R_{wp} (weighted residual factor) and GOF (goodness of fit) values from Rietveld analysis are listed. (**D** and **E**) Scanning electron microscopy (SEM) images of $FeO_{0.3}F_{1.7}$ and $FeO_{0.7}F_{1.3}$. (**F** and **G**) X-ray photoelectron spectra (XPS) of Fe 2p and O 1s for $FeO_{0.3}F_{1.7}$ and $FeO_{0.7}F_{1.3}$. a.u., arbitrary units.

as indicated from the lattice strips of its (012) plane (fig. S3E). The lattice oxygen at grain surface/subsurface is likely prone to escape with the preservation of Fe—F lattices, resulting in O-deficient component near the surface. This effect is potentially associated with the appearance of a hollow structure in view of the O debonding–induced etching process, which is also observed from SEM (Fig. 1E). The high-angle annular dark-field scanning transmission electron microscopy (HAADF-STEM; fig. S3D) further discloses the element distribution mapping of individual particle and its surroundings. The distribution of O element is consistent with those of Fe and F, and they collectively profile a rhombus shape, which is a two-dimensional projection of octahedral grain of oxyfluoride. The

homogeneous oxygen distribution in our rutile structure should benefit from the inherent doping (from hydration water molecules in precursor) instead of outside-in penetration by extrinsic oxygen source. Chemical homogeneity could effectively weaken Li diffusion barrier in mixed anion rutile framework with anisotropic diffusion channels (*31*). The spatial distribution of C and B elements expectedly conforms with the wrapping behavior of surrounding KB wires and IL capping. Similar rhombus shape is also profiled by existing N element mapping, demonstrating the structure-directing effect of imidazole cation during IL-induced fluoride precipitation (*26*). The weight content of electroactive fluoride compositions is estimated to be as high as ~74%, according to thermogravimetric analysis (TGA) in an oxygen flow with the final product assumed as Fe_2O_3 (fig. S4).

The x-ray photoelectron spectra (XPS; Fig. 1, F and G, and fig. S5) disclose that both the oxyfluorides have two different bonding states in Fe 2p, including O—Fe^{3+}—F/Fe^{2+}—F for dominant rutile phase and Fe^{3+}—F for residual fluoride, corresponding to the peaks at 711.6 and 714.3 eV for Fe $2p_{3/2}$ (*32*, *33*). Another shoulder peak at higher binding energy of 717.8 eV should be attributed to satellite feature formed by an incorporated shake-up process of high-spin Fe species (*33*). Note that the fraction of O—Fe^{3+}—F for $FeO_{0.7}F_{1.3}$ is apparently higher than for $FeO_{0.3}F_{1.7}$, agreeing with the more pronounced Fe—O signal (at 530.3 eV in O 1s) for the former (*33*). These results are in accordance with their O doping degrees. The other oxygen-containing peaks are around 531.9 and 533.2 eV, which are assigned to C—O bonding and absorbed moisture from atmosphere (*34*). The C—O bonding may stem from the thermal-induced O doping in IL capping (or carbon wires) or its surface interaction with lattice oxygen. The contribution of hydration water of HTB minor phase in $FeO_{0.3}F_{1.7}$ seems difficult to be picked out due to its approximate location with exotic H_2O peak (*35*). The C 1s spectra can be deconvoluted into three peaks at 284.8, 285.7, and 286.5 eV, denoting different hybridization states of C—C/C═C, C—N (from residual IL capping), and C—O (*36*, *37*). For F 1s spectra, the signal at 685.3 eV is attributed to the F^- bonding with iron (*33*). The higher doping degree of electrophilic O atoms motivates a slight shift of Fe—F signal toward lower binding energy.

Characterization of solid-liquid F-transport channel

On the basis of density functional theory (DFT) method, electrostatic potential (ESP) analysis was performed to visualize the charge distribution of the TPFPB molecule (Fig. 2A). TPFPB has an electron-deficient boron center (bright red area), which exhibits a strong attraction to electron-rich fluorine with a binding energy of −3.39 eV (Fig. 2B and table S2). TPFPB with F-binding affinity favorably promotes LiF splitting via the formation of TPFPB-F complex, as indicated by the notably reduced dissociation energy (Fig. 2C and table S3). The LiF dissociation ability of TPFPB is further confirmed using inductively coupled plasma optical emission spectrometer (ICP-OES), as shown in table S4. According to the Li^+ concentration below the detection limit, LiF with high dissociation energy is almost insoluble in 1,2-dimethoxyethane (DME) alone. In contrast, TPFPB can react with LiF in a stoichiometric ratio close to the theoretical value of 1:1, leading to the release of mobile Li^+ and the formation of solvated $[TPFPB\text{-}F]^-$ complex.

To further characterize the solvated $[TPFPB\text{-}F]^-$ intermediate, nuclear magnetic resonance (NMR) spectroscopy and Fourier transform infrared (FTIR) spectroscopy measurements were carried out with the pristine TPFPB as a control. In the ^{19}F NMR spectra (Fig. 2D), there is a signal that emerges in the upfield region with a chemical shift (δ) of −192.2 parts per million (ppm) in the case of TPFPB-LiF/DME. This δ value is very close to that of the dissolved LiF (fig. S6), and it validates the generation of dissociated F^- by the anion acceptor. The favorable coordination with electron-rich F^- increases the electron density of the surrounding fluorine on TPFPB molecular, as indicated by the color spreading around the blue center in the ESP image of TPFPB-F (Fig. 2A). This phenomenon would trigger the enhancement of the shielding effect, which is responsible for the upfield shifts of some ^{19}F signals belonging to TPFPB. The interaction between TPFPB and F could be further verified by the FTIR measurement (fig. S7). After the LiF-induced fluorination, the peaks at 1645, 1519, and 1467 cm^{-1} associated with the fluorinated benzene ring of the TPFPB shift to the lower wave numbers (*38*). The red shift occurrence is consistent with the concomitant energy reduction by the conversion from TPFPB to TPFPB-F complex. These results demonstrate that the TPFPB molecule as F^- receptor enables the F-state transformation from the solid LiF lattice to the solvated $[TPFPB\text{-}F]^-$ intermediate.

For the Li-driven Fe—F conversion system, the dissolved F^- tends to react with the oxidized Fe species in the reconversion process. To evaluate the kinetics impact of solvated $[TPFPB\text{-}F]^-$ intermediate on the reconversion to FeF, the DFT calculations were performed to further investigate the reaction process of LiF—Fe system without and with the assistance of TPFPB. Here, the climbing image nudged elastic band (CI-NEB) method was used to simulate the potential F-transport pathways and calculate the corresponding energy barriers (*39*). To simplify the calculation models, the F atom is set to break away from the initial Li—F and bond with Fe atom finally. As seen in Fig. 2E, the direct conversion between solid LiF and Fe requires to overcome a high energy barrier of 7.19 eV and terminates in the form of free Li and Fe—F. The introduction of TPFPB to the LiF—Fe system develops an alternative reaction pathway involving the TPFPB-F intermediate. The reaction energy barrier (5.28 eV) is substantially reduced when the dissolved F^- preferentially attaches to TPFPB first, and it is further decreased to 3.66 eV when F^- transfers from $[TPFPB\text{-}F]^-$ to Fe species finally. These reduced energy barriers under the assistance of TPFPB could kinetically promote the F sublattice conversion (from Li—F to Fe—F). Therefore, the solvated F^- intermediate of $[TPFPB\text{-}F]^-$ interacts with solid discharge products at interphase interface, enabling the construction of a solid-liquid "F-transport channel" (Fig. 2F). This fluid channel further improves the original rough solid-solid contact and enables the energetically favorable F-ion transport from LiF toward Fe species. It is expected to achieve a facile Li^+ extraction and host structure reconstruction during charge. This F-transport channel can function as the role of catalyst, because the TPFPB molecule is not consumed in the solid-liquid conversion pathway.

Electrochemical performance of $FeO_{0.3}F_{1.7}$ and $FeO_{0.7}F_{1.3}$ cathodes

To evaluate the effect of TPFPB additive on electrochemical behavior of fluoride cathode, 0.05 M TPFPB together with a certain amount of LiF is added into DME containing 1.0 M lithium bis(trifluoromethanesulfonyl)imide (LiTFSI), denoted as LiTFSI-LiF-TPFPB/DME. The concentration optimization of the crucial TPFPB-LiF additive pair is discussed later. Two types of conventional electrolytes of ether solution (1 M LiTFSI in dioxolane and DME, denoted

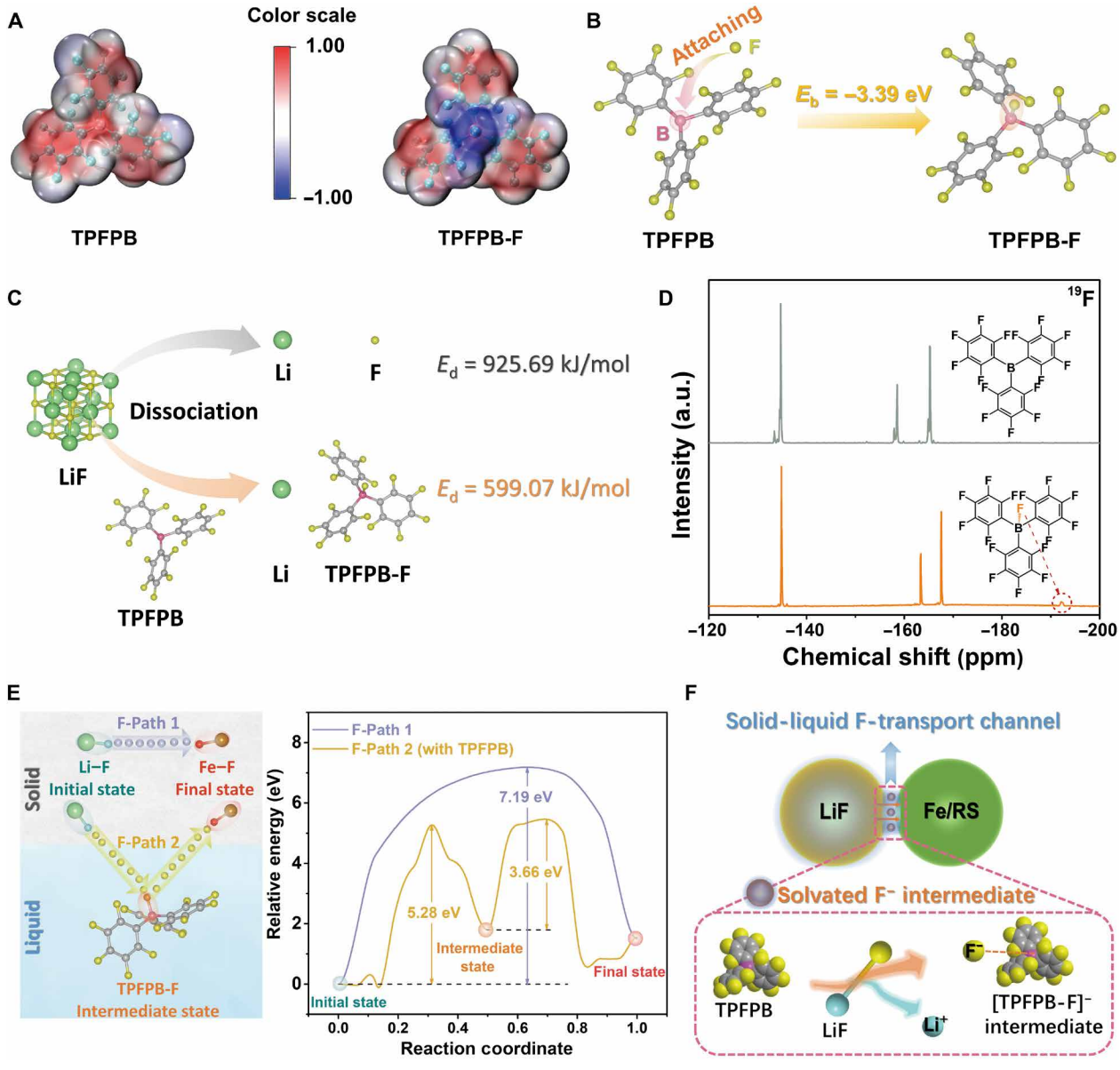

Fig. 2. Characterization of solid-liquid F-transport channel enabled by TPFPB. (**A**) Molecular structures and calculated ESP images of TPFPB and TPFPB-F complex. (**B**) Structural configurations and binding energy of F atoms attaching to TPFPB by DFT calculation. (**C**) Graphic representation of LiF dissociation energy values under the cases without and with anion acceptor TPFPB based on DFT calculation. (**D**) ^{19}F NMR spectra of TPFPB/DME (top) and TPFPB-LiF/DME (bottom) solutions. (**E**) Possible F-transport pathways and corresponding energy barrier profiles for F-state transformation from Li—F to Fe—F without and with the assistance of TPFPB. (**F**) Illustration of construction of solid-liquid F-transport channel between LiF and Fe species [e.g., metallic iron and rock salt (RS) phase] mediated by solvated $[TPFPB\text{-}F]^-$ intermediate at multiphase interfaces.

as LiTFSI/DOL-DME) and carbonate solution [1 M lithium hexafluorophosphate ($LiPF_6$) in ethylene carbonate (EC) and dimethyl carbonate (DMC), denoted as $LiPF_6$/EC-DMC] were also tested as control experiments. The Li-driven conversion reaction of $FeO_{0.3}F_{1.7}$ cathode is activated in a potential range of 1.2 to 4.0 V (fig. S8). The initial lithiation of $FeO_{0.3}F_{1.7}$ involves a constant two-stage insertion reaction above ~1.8 V and subsequently incorporative conversion of lithiated (oxy)fluorides corresponding to a prolonged quasi-plateau within the voltage range of 1.8 to 1.2 V (fig. S8A) (*13*, *40*). Then, the conversion products (e.g., LiF, Li_2O, and Fe) are sequentially oxidized to Fe^{2+}/Fe^{3+}-containing (tri)rutile/rock salt phases (e.g., Li_xFeF_3, FeO_xF_{2-x}, and $Li_nFeO_xF_y$) during charge process (*7*, *15*). Further cycling of $FeO_{0.3}F_{1.7}$ causes the evolution into two distinct raised plateaus in both discharge and charge curves, corresponding to two couples of cathodic/anodic peaks (around 3.1/3.3 and 2.0/2.8 V) in cyclic voltammetry (CV) curves (fig. S9). Compared with the sharp redox peaks at lower voltages in ether-based cells, the corresponding peaks show much wider profiles with smaller current response and larger overpotential when cycled in $LiPF_6$/EC-DMC. This comparison indicates the advantage of conversion kinetics for ether

electrolyte system. TPFPB additive enables a further shrinkage of gap between cathodic and anodic peaks for conversion process involving LiF splitting. Correspondingly, a shifting of anodic peak toward lower voltage with the reduction of polarization overpotential to a lowest value of 797 mV is observed in TPFPB-containing ether system (fig. S9).

By experiencing multiple-electron transfer, $FeO_{0.3}F_{1.7}$ in both ether-based electrolytes achieves the high initial capacities exceeding 600 mAh/g at 100 mA/g, higher than that in carbonate electrolyte (Fig. 3A). Impressively, TPFPB addition enables a high capacity retention for $FeO_{0.3}F_{1.7}$ even with capacity-upward tendency during the following cycling. This activation phenomenon likely benefits from the construction of solid-liquid F-transport channel. There, the "dead" LiF accumulated in early cycles is gradually revived, boosting an elevated and prolonged conversion plateau from 10th to 30th cycles. The voltage polarization almost does not degrade within 50 cycles, whereas that deteriorates seriously in cases of control carbonate- and ether-based cells (fig. S8, C and E). Note that the slight predissolved LiF into TPFPB-containing electrolyte appears to be helpful in preventing lattice-F dissolution by mitigating its concentration

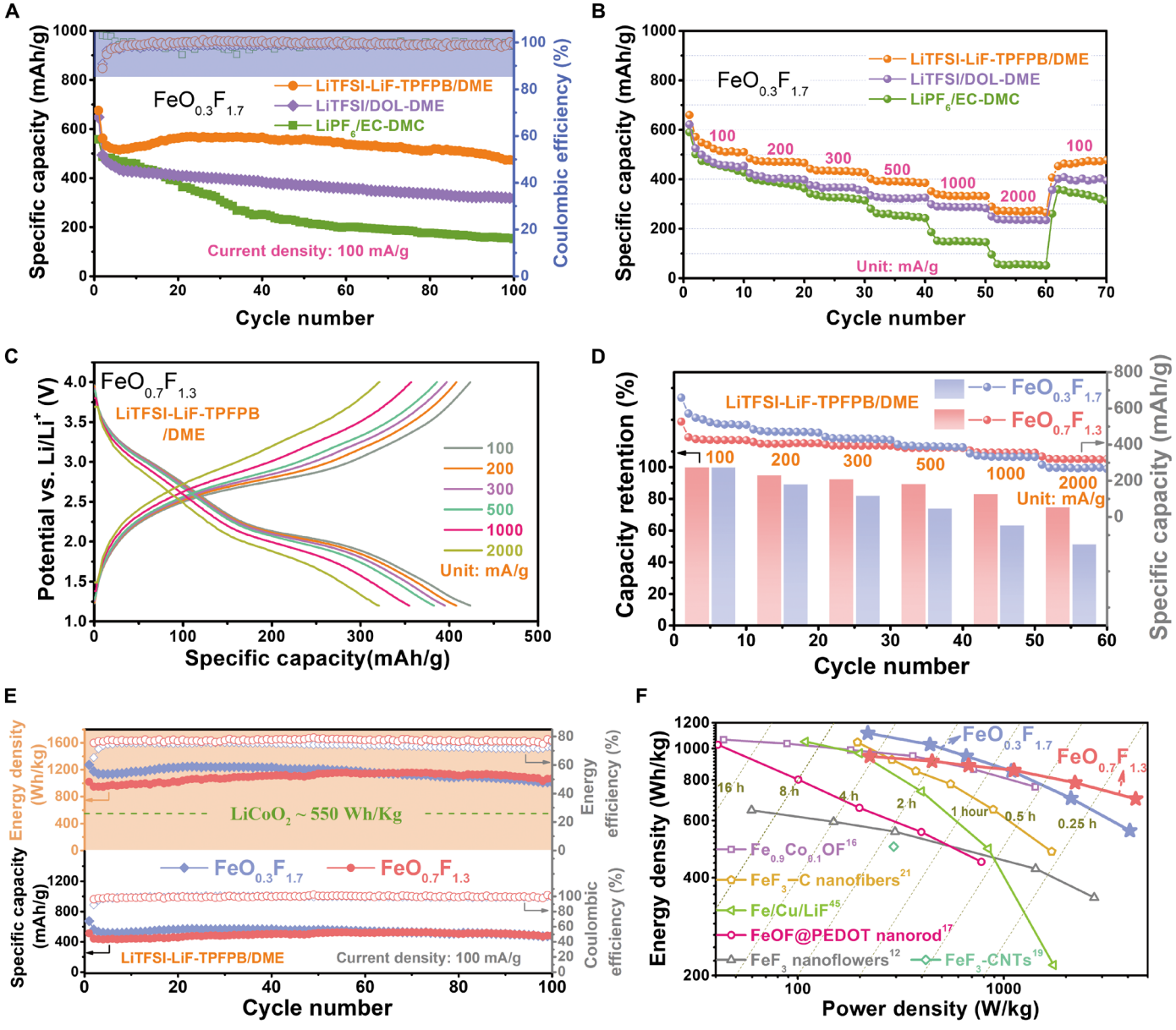

Fig. 3. Electrochemical performance of $FeO_{0.3}F_{1.7}$ and $FeO_{0.7}F_{1.3}$ cathodes. (**A**) Cycling performance and coulombic efficiencies of Li/$FeO_{0.3}F_{1.7}$ cells with different electrolytes of LiTFSI-LiF-TPFPB/DME, LiTFSI/DOL-DME, and $LiPF_6$/EC-DMC at 100 mA/g. (**B**) Rate performance of Li/$FeO_{0.3}F_{1.7}$ cells based on different electrolytes. (**C**) Galvanostatic discharge/charge profiles of $FeO_{0.7}F_{1.3}$ cathode in LiTFSI-LiF-TPFPB/DME electrolyte depending on various current densities from 100 to 2000 mA/g. (**D**) Comparison of rate performance and corresponding capacity retention ratio at various rates for both iron oxyfluorides. (**E**) Discharge capacity/coulombic efficiency and corresponding energy density/energy efficiency as a function of cycle number for both iron oxyfluoride cathodes at 100 mA/g. (**F**) Ragone plots of Li/$FeO_{0.3}F_{1.7}$, Li/$FeO_{0.7}F_{1.3}$ cells, and some reported Li/iron (oxy)fluoride batteries. Both energy and power densities are calculated on the basis of the weight of active material.

gradient. It may also serve as extra F source to promote the reoxidation of Fe in rutile phase with higher valence state, contributing to the capacity recovery as well. The reversible capacity of $FeO_{0.3}F_{1.7}$ is still preserved at 472 mAh/g after 100 cycles. In contrast, in conventional carbonate and ether systems, the reversible capacities drop seriously and are below 200 and 400 mAh/g after 100 cycles, respectively. The capacity fading is associated with the blurring of two-stage plateaus, likely indicating the weakened ordering of Fe—F (O) lattice arrangement as a consequence of the accumulation of passive amorphous LiF or various surface defects (e.g., by Fe/F dissolution or side reaction) (*41*). It appears that only carbonate or ether moieties are unable to build effective CEI layer to retard structure disordering, particle clustering, and active material dissolution (e.g., Fe- or F-based species) (*18*, *19*). The adoption of $LiPF_6$ salt is not favorable in view of the potential formation of undesired decomposed products such as HF and PF_3O, which are detrimental to many cell components (*42*). The construction of solid-liquid F-transport channel also endows $FeO_{0.3}F_{1.7}$ with the most superior-rate performance (Fig. 3B and fig. S8B). The reversible capacities are as high as 470, 432, 389, 334, and 271 mAh/g at 200, 300, 500, 1000, and 2000 mA/g, respectively. The typical two-stage lithiation plateaus can be well maintained without serious voltage drop even under a current density up to 1000 mA/g. Note that the addition of giant TPFPB molecules around the solvated Li would more or less increase the viscosity of electrolyte and decrease its bulk ion mobility (*43*). This effect would partially balance out the improved reaction kinetics (benefitting from solid-liquid F-transport channel) particularly under ultrafast charge-discharge. The KB-only cathode in LiTFSI/DOL-DME delivers a capacity of less than 50 mAh/g with slope charge-discharge curves (fig. S10), indicating its negligible capacity contribution to fluoride composite cathode.

The rutile structure iron oxyfluorides can perform varying Li storage performance depending on the componential O/F ratio (*13*). To confirm the impact of O content increase on electrochemical behavior, $FeO_{0.7}F_{1.3}$ is also cycled in different candidate electrolytes (Fig. 3C and fig. S11). Similar trends are seen for the Li/$FeO_{0.7}F_{1.3}$ cells in terms of cycling capability and rate performance. Figure S11A shows the galvanostatic profiles of $FeO_{0.7}F_{1.3}$ cycled in LiTFSI-LiF-TPFPB/DME at 100 mA/g. During the initial lithiation, a similar curve as that of $FeO_{0.3}F_{1.7}$ is observed. The increase of Fe^{3+} content in FeO_xF_{2-x} with deeper O doping contributes to the developing of intercalation reaction located around 2.4 V. This deeper O doping certainly improves its intrinsic electronic conductivity (*13*) and, therefore, could boost the Li diffusion toward core lattices and the flatting of reaction plateaus. The substitution of O^{2-} for F^- in FeO_xF_{2-x} with concomitant increase of the oxidation state of iron does not achieve more electron transfer in the set voltage range. The content reduction of (near-)complete-conversion Fe—F domains is associated with the decrease of initial discharge capacity for $FeO_{0.7}F_{1.3}$ compared with $FeO_{0.3}F_{1.7}$. Upon the subsequent charge, only a rough plateau without evident multistage process can be observed. This discrepancy indicates that the divided delithiations to O/F-rich phases probably proceed simultaneously (*16*). The converted Fe and LiF products should mainly participate in the formation of F-rich rutile. In the following cycles, the discharge curve exhibits two-stage upward sloped plateaus, corresponding to two reduction peaks centered at ~3.0 and ~1.9 V in CV profiles (fig. S12). In comparison with $FeO_{0.3}F_{1.7}$, the broader cathodic peak at high voltage for $FeO_{0.7}F_{1.3}$ is in line with its strengthened intercalation. However, the subsequent lithiation peak correlated with extrusion/conversion reaction shifts to the lower potential, which should be ascribed to the overall change of Fe—O(F) bond ionicity with the increase of O content in the $Li_yFeO_xF_{2-x}$ structure (*13*). The inverse delithiation reaction proceeds with an amplified anodic peak at approximately 2.7 V. The disappearance of high-voltage anodic peak indicates the suppression effect on the regeneration of Fe^{3+}—F moieties due to sufficient O doping in $FeO_{0.7}F_{1.3}$.

With the activation of LiF via solid-liquid F-transport channel, the $FeO_{0.7}F_{1.3}$ cathode also exhibits the progressive raise of lithiation plateaus (especially for the conversion region) and, therefore, overpotential mitigation. Its capacity gradually increases and exceeds 500 mAh/g within 50 cycles (fig. S11A). The distinct two-stage lithiation plateaus can be well preserved even when the current density increases up to 2 A/g (Fig. 3C). There, the overpotential does not seriously compromises in the rigorous rate test, and it only increases from 668 mV at 100 mA/g to 834 mV at 1000 mA/g, which is smaller than that for $FeO_{0.3}F_{1.7}$ at the same rate (fig. S13). The rate performance of $FeO_{0.7}F_{1.3}$ is accordingly improved with high capacity values of 355 and 320 mAh/g and capacity retention ratios of 83 and 75% at 1 and 2 A/g, respectively (Fig. 3D), surpassing those for $FeO_{0.3}F_{1.7}$. In the long cycling process (Fig. 3E), $FeO_{0.7}F_{1.3}$ also experiences a longer capacity-boosting period and achieves a comparative reversible capacity of 484 mAh/g (at 100 mA/g) after 100 cycles as that of $FeO_{0.3}F_{1.7}$. This capacity release corresponds to an energy density as high as 1068 Wh/kg, about double the theoretical energy density of the $LiCoO_2$ cathode (550 Wh/kg). Note that the superior polarization performance for conversion-type $FeO_{0.7}F_{1.3}$ results in a sustaining high round-trip energy efficiency approaching to 80%, which overcomes the intrinsic issue of low energy efficiency (<60%) for general metal fluoride systems with sluggish conversion kinetics (*7*, *44*). From the Ragone plots in Fig. 3F, our Li/FeO_xF_{2-x} cells both show the evident improvement of energy and power densities (based on the weight of active materials), compared with previous reports on (oxy)fluoride cathodes even with the assistance of intentional nanoengineering and extra conductive wiring (*12*, *16*, *17*, *19*, *21*, *45*). In particular, they perform the superior energy densities of 1100 Wh/kg for $FeO_{0.3}F_{1.7}$ and 700 Wh/kg for $FeO_{0.7}F_{1.3}$ under the power densities of 220 and 4300 W/kg, respectively. The key to the performance progress lies in the accurate dual modulation of doping content and electrolyte formula. The further introduction of oxygen into the oxyfluoride core structure not only effectuates the penetration of electron-conduction hinge but also adjusts the conversion phases that reduce the precipitation of inter-LiF and stabilize the secondary parent phase of O-rich rock salt. Moreover, the higher crystallinity with more regular F/O arrangement is favorable for lattice Li diffusion and mechanical stability (*31*). These factors are responsible for the more lasting and efficient bulk redox reaction of $FeO_{0.7}F_{1.3}$.

Note that the electrolyte injected in each cell only contains ~1.125×10^{-6} mol of dissolved F^- (based on a lean electrolyte volume of 25 μl and the dissolved LiF concentration of 0.045 mol/liter from the ICP result). Assuming that all the dissolved F^- participates in the reaction with Fe-based species, we recalculate the specific capacity of $FeO_{0.3}F_{1.7}$ based on the total weight of active materials in cathode and electrolyte (fig. S14). As seen, there is no obvious reduction of gravimetric capacity value after taking the possible active material of dissolved LiF into account. To evaluate the electrochemical stability of the F-transport channel during cycling, the ^{19}F NMR measurement on the pristine and cycled LiTFSI-LiF-TPFPB/DME

electrolyte was performed (fig. S15). In the case of pristine electrolyte, apart from the signals associated with the solvated F^- intermediate $[TPFPB\text{-}F]^-$, a strong peak arising in the relatively downfield region (δ = −79.4 ppm) should be ascribed to the existence of high-concentration $TFSI^-$ anion. The addition of LiTFSI salt does not influence the interaction environment in $[TPFPB\text{-}F]^-$ in view of the unchanged chemical shifts of its characteristic signals. After cycling, all the ^{19}F signals still keep their respective chemical shifts with tiny variation (<0.2 ppm). Because it is inevitable to dilute the residual electrolyte adsorbed in the separator when preparing the cycled sample for NMR measurement, these signals are correspondingly weakened and that of dissociated F^- (δ = −192.2 ppm) is prone to be covered by the background signal. This result indicates that the TPFPB-containing electrolyte can keep the stable formulation and coordination situation during cycling, including the crucial $[TPFPB\text{-}F]^-$ complex. Consequently, the endurable F-transport channel could contribute to the superior cycling performance of iron oxyfluoride cathodes (Fig. 3E).

To optimize the F dissociation effect, we also consider the different concentrations of TPFPB/LiF additives. Because the strong Lewis acidity of TPFPB would initiate the ring-opening polymerization of 1,3-dioxolane (DOL), DME is used as the only ether solvent in TPFPB-containing electrolyte (*46*). The linear molecule of DME with high donicity gives rise to the strong coordination with Li^+ (*47*), which could promote the higher reactivity of additive toward the splitting of LiF. Note that the stable cell voltage is above 3.0 V before cycling in all TPFPB-containing conditions, as our "F-receptor" is much harder to break Fe—F bonds in cathode lattice than to split LiF (*25*). As shown in fig. S16A, the LiTFSI/DME electrolyte with 0.05 M TPFPB appears brownish yellow. This solution mixing with LiF undergoes the decoloration process induced by the complexion reaction of TPFPB and LiF. The excess LiF addition could guarantee the sufficient fluorination of anion acceptor in the case of 0.05 M TPFPB–0.5 M LiF. To evaluate the electrochemical stability of candidate electrolytes with different TPFPB/LiF additives, a single-cycle CV was performed in coin cells with Al and Li foils as the working and counter electrodes at a scan rate of 2 mV/s (fig. S16B). During the first cathodic scan to 1.2 V, the cell without LiF addition shows the evidently higher baseline current response and a following peak of around 1.2 V, most likely due to the reduction of TPFPB with the electron-withdrawing pentafluorophenyl group (*25*). This phenomenon is effectively suppressed when TPFPB is prefluorinated via splitting LiF and complexing fluoride anion, as indicated by the reduction of baseline current with the increase of LiF addition. One can also note that the charge density around the electron-deficient boron would be increased substantially when the electron-rich fluorine attached to TPFPB (Fig. 2A). Therefore, the $[TPFPB\text{-}F]^-$ complex with negative charge exhibits less tendency to accept extra electrons and to be reduced, compared with the TPFPB-alone case. In the following oxidation process, the electrolyte with 0.5 M LiF could endure a highest stable voltage up to ~5.0 V before a booming anodic current appears. There, the oxidation of ether solvent or anodic corrosion of Al collector by imide-based salts is prone to occur (*42*, *48*). Note that the onset of oxidation in LiF-free electrolyte is pushed back to a much lower voltage of ~4.1 V. These results indicate that precomplexation of TPFPB molecules helps to improve the electrochemical stability of electrolyte. $FeO_{0.3}F_{1.7}$ cathodes in all the TPFPB-containing electrolytes perform similar lithiation/delithiation behavior during the initial cycle, apart from an extra quasi-plateau tail below 1.5 V in the cases with 0 and 0.05 M LiF (fig. S16C), corresponding to the incomplete cathodic peaks in their CV profiles (fig. S16B). As the cycle goes on, this particular plateau continues to extend and is accompanied with the flattening of the charge curve above 3.5 V, which is likely caused by TPFPB-induced electrolyte decomposition. This effect brings out an unusually transient capacity growth but is followed by a rapid cell degradation with CE fluctuation, plateau disappearance, and polarization increase (fig. S16, D to F). In sharp contrast, the optimized cell with 0.05 M TPFPB–0.5 M LiF has excellent cycling stability with typical fluoride-activated curves and steady CE values approaching to 100%. Overall, the proper combination of TPFPB and LiF in the DME-based system enables the improved electrochemical performance of fluoride cathode and notably mitigation of electrolyte decomposition.

Reaction kinetics of $FeO_{0.3}F_{1.7}$ in various electrolytes

The electrolyte type has a substantial impact on the reaction kinetics of fluoride during cycling due to their interactions with cathode. Figure S17 displays the evolution of electrochemical impedance spectra (EIS) of pristine and cycled Li/$FeO_{0.3}F_{1.7}$ cells at different cycling stages. Nyquist plots of various cells show the near-completed semicircle in a high-frequency range, representing the interface resistance R_i, containing the contributions of cathode/anode-electrolyte interface film resistance R_f and charge transfer resistance R_{ct}. The minor arc in middle frequencies corresponds to the semi-infinite Warburg impedance Z_w caused by the solid-state diffusion of Li. The low-frequency inclined straight line is associated with the diffusion and accumulation of Li, denoting finite-length Warburg impedance Z_{flw} (*49*). The intercept before the start of semicircle can be assigned to the bulk electrolyte resistance (R_e), which does not undergo evident variation with the progress of cycling, suggesting the absence of undesirable electrolyte degradation for all the cases. The cell with LiTFSI-LiF-TPFPB/DME electrolyte shows the most stable evolution of interfacial resistances without remarkable increase after 50 cycles, probably benefiting from the in situ building of effective CEI by F-activated additive. The degradation of R_i values cannot be suppressed for the control cells especially in carbonate electrolyte in view of the accumulation of passivated LiF. The impedance evolutions of cells with respective electrolytes are in accordance with the corresponding cycling performance.

CV measurement for $FeO_{0.3}F_{1.7}$ cathode at different scan rates was performed to emphasize the kinetic advantage in LiTFSI-LiF-TPFPB/DME (fig. S18). Representative CV curves all exhibit the pairs of redox peaks associated with the intercalation and conversion processes. The overall CV shape could be preserved well with the increase of scan rates, favoring the estimate of pseudocapacitance contribution. The measured current response (i) as a function of potential (V) obeys a power law relationship with scan rate (v): $i(V) = av^b$, where a and b are the adjustable parameters (*50*). The b value is determined from the slope of the plots based on the deduced expression of log $i(V) = b \log v + \log a$, and those derived from respective CV peak positions are shown in fig. S18B. In view of the overpotential change with the scan rate, the independent variable potential should be slightly adjusted on the basis of the equidistribution principle. The b value close to 1.0 is indicative of a capacitance-dominated response, whereas it is close to 0.5 when a diffusion-controlled behavior (i.e., faradaic intercalation) dominates (*51*). The near-linear fitting of log i – log v plots is obtained in the whole rate range, and the b values for the redox peaks at high-voltage positions are approaching 1.0 in all the cases (especially for ether-based electrolytes). The topotactical

transformation to a disordered solid solution phase by random Li^+ occupation without the interruption of M-F bonds is responsible for the high pseudocapacitance contribution (*41*, *52*). The interfacial charge transfer in the following conversion reaction certainly contributes to the higher-fraction diffusion-controlled processes, as indicated by the lowering of *b* value (around 0.7 to 0.8). The nanoscale effect and topological relationship between bulk F sublattices of metal fluoride and LiF do not cause a notable decrease of *b* values (*53*, *54*). The ratio of capacitive contribution can be quantitatively evaluated according to the equation $i(V) = k_1v + k_2v^{1/2}$, where the *i* value is the combinational contributions from capacitance effect (k_1v) and intercalation process ($k_2v^{1/2}$). Figure 4A displays a typical CV curve at 0.6 mV/s, where the capacitive current (k_1v) is integrated into an orange region and distinguished from the total current ($k_1v + k_2v^{1/2}$). In LiTFSI-LiF-TPFPB/DME, the ratio of capacitive contribution of $FeO_{0.3}F_{1.7}$ to total stored charge reaches a high value of around 75 to 86% at various scan rates, evidently higher than the cases of LiTFSI/DOL-DME and $LiPF_6$/EC-DMC (Fig. 4B). This positive effect benefits from the increase of surface reaction sites activated by the interfacial solid/liquid F-transport channel.

The diffusion coefficient (*D*) varies as a function of lithiation degree of electrode (with respect to reaction voltage), as estimated by means of galvanostatic intermittent titration technique (GITT) in Fig. 4C and fig. S19 (*7*). All the cells are precycled at 100 mAh/g for 10 cycles to achieve reversible phase conversion before GITT measurement. Then, they are applied under a weaker current pulse of 35 mA/g for an intermittent time (τ) of 1 hour (3600 s), followed by an open-circuit relaxation of 6 hours to allow the system to reach a (quasi-)equilibrium state. The sequence of current pulse and relaxation process is repeated until the full discharged/charged state. The electrochemical process of driven cation follows the second Fick's law of diffusion. Because the transient potential (E_τ) displays a linear relationship with the square root of τ (fig. S19, D and E), the *D* value can be calculated by a simplified equation (*55*)

$$D = \frac{4}{\pi\tau}\left(\frac{m_B V_m}{M_B S}\right)^2 \left(\frac{\Delta E_S}{\Delta E_\tau}\right)^2 (\tau \ll L^2/D)$$

where m_B, M_B, and V_m are the mass, molecular weight (92.87 g/mol), and molar volume (2.13×10^{-5} m^3/mol) of $FeO_{0.32}F_{1.68}$, respectively; *L* and *S* are the thickness and area of electrode, respectively; ΔE_S is the difference of open circuit voltages after two adjacent relaxations; and ΔE_τ is the voltage difference between the beginning and termination of one single GITT step. From the evolution of *D* values, $FeO_{0.3}F_{1.7}$ expectedly performs a faster Li diffusion proceeding in intercalation reaction than in conversion reaction during discharge, with a minimization of *D* value at the intercalation-to-conversion transition position (around 2.3 V), where the interface transport becomes dominant with the occurrence of substantial multiphase nucleation and growth (*5*). In the delithiation process, the accumulated Li^+ at the activated fluoride (sub)surface tends to break free from solid lattices faster due to shorter migration path and higher

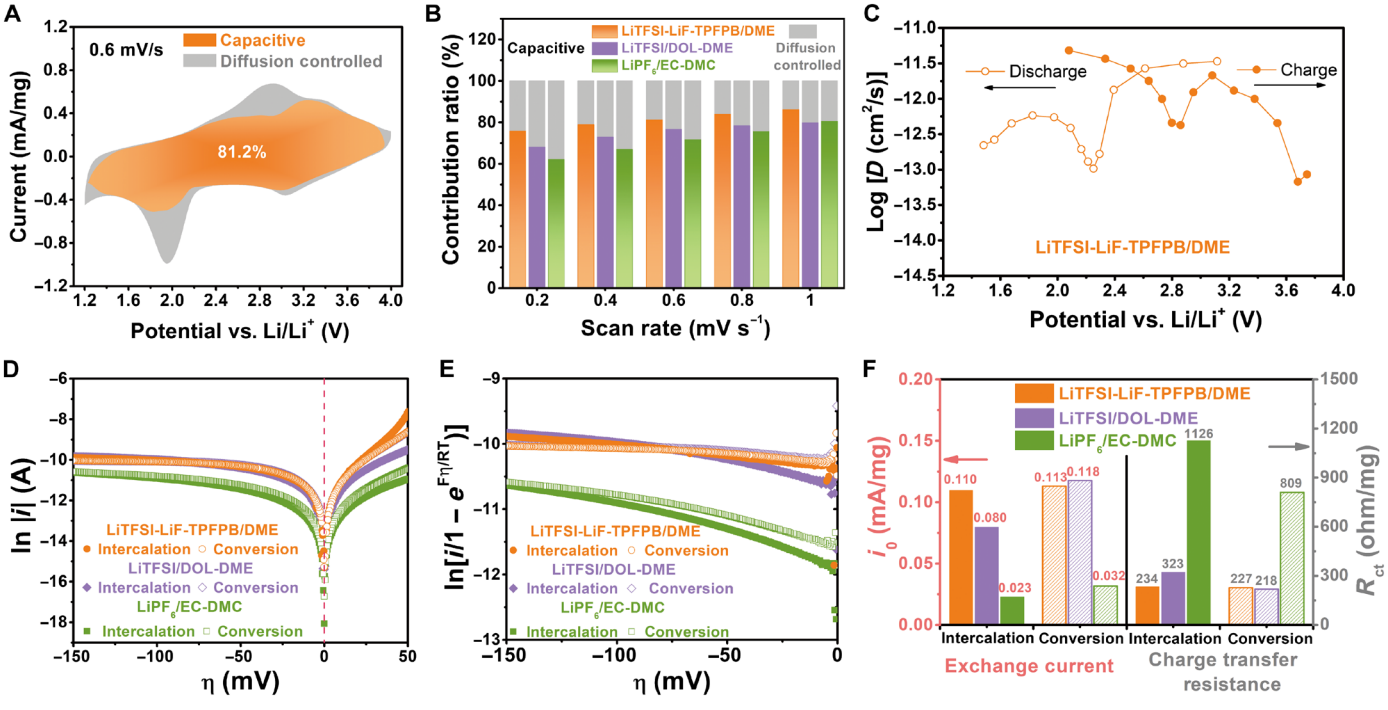

Fig. 4. Reaction kinetics of $FeO_{0.3}F_{1.7}$ in various electrolytes. (**A**) CV curve of $FeO_{0.3}F_{1.7}$ cathode using electrolyte of LiTFSI-LiF-TPFPB/DME at 0.6 mV/s with divisional capacitive contribution (k_1v; orange area) and diffusion-controlled contribution ($k_2v^{1/2}$; gray area) based on $i(V) = k_1v + k_2v^{1/2}$. (**B**) Column graphs of scan rate–dependent charge storage contributions from both capacitive and diffusion-controlled processes for Li/$FeO_{0.3}F_{1.7}$ cells with various electrolytes. (**C**) Diffusion coefficient (*D*) plots estimated from galvanostatic intermittent titration technique (GITT) as a function of reaction potential during discharge and charge for Li/$FeO_{0.3}F_{1.7}$ cell in LiTFSI-LiF-TPFPB/DME electrolyte. (**D**) Tafel plots of $FeO_{0.3}F_{1.7}$ cathode in various electrolytes at intercalation and conversion plateaus during lithiation process. (**E**) Corresponding Allen-Hickling plots with intercepts on vertical axis to determine exchange current. (**F**) Comparison of calculated exchange current and charge transfer resistance in different electrolyte systems and intercalation/conversion stages. All Tafel tests were performed at 25°C.

concentration gradient. Therefore, the relatively high D values are obtained at the early stage of charge. The local minimization of D value (around 2.8 V) still exists during Li extraction. The D values of $FeO_{0.3}F_{1.7}$ in TPFPB-based electrolyte fluctuate from 5×10^{-12} to 5×10^{-13} cm^2/s in most of the voltage range. The distribution of D values discloses the asymmetry and complication of conversion paths during charge and discharge (*5*). In all the electrolyte systems, the D values of $FeO_{0.3}F_{1.7}$ undergo similar evolution tendency (fig. S20). The D values in carbonate electrolyte fluctuate from 10^{-12} to 10^{-15} cm^2/s depending on different voltages, which are lower than those in the cases of two ether-based electrolytes. This inferior reaction kinetics is likely ascribed to the formation of thick and discontinuous CEI layer on the cycled fluoride in carbonate electrolyte (*18*), leading to the hindered mass transport across cathode-electrolyte interface, which is also indicated by the serious interfacial resistance for carbonate electrolyte in EIS results (fig. S17). Note that this cell based on TPFPB-based electrolyte does not suffer serious potential hysteresis (η) from the steady-state (quasi-equilibrium) voltage plots. The η value at the 50% state of full charge/discharge (roughly in the conversion plateau region) is as small as 480 mV, which is much lower than that (700 mV) in the case of carbonate electrolyte (fig. S19C).

To further evaluate the electrochemical kinetics especially at the equilibrium of faradaic activity, we used an unconventional technique of Tafel analysis (*56*), which has never been applied to fluoride cathodes as far as we know. Typical Tafel behaviors are observed in all the $FeO_{0.3}F_{1.7}$-based systems as shown in Fig. 4D. An important term named as exchange current (i_0) is measured at equilibrium potential (when the normalized overpotential is zero) by Tafel analysis. It represents a contributing factor to voltage polarization and electrode reaction rate. The cathodic Tafel equation is given as follows

$$\eta = \frac{RT}{\alpha F}\ln i_0 - \frac{RT}{\alpha F}\ln i$$

where η denotes the polarization; R and F represent the gas constant and Faraday's constant, respectively; T is the absolute temperature (298.15 K); and α is the charge transfer coefficient. A linear relation exists between logarithmic current and polarization in a strong polarization region, where the voltage is far enough from the equilibrium state. The Tafel results were replotted in Fig. 4E according to Allen-Hickling plots based on the Butler-Volmer equation given below

$$\ln\left[i/\left(1 - e^{\frac{F\eta}{RT}}\right)\right] = \ln i_0 - \frac{\alpha F}{RT}\eta$$

There, the exchange current is determined by the vertical axis intercept of the extrapolated linear fitting of Allen-Hickling plots. In all the electrolyte systems, the exchange current in the conversion region is comparable to that in the intercalation region (Fig. 4F). The formation of metallic conductive network via conversion reaction enhances the spatial electron percolation and accordingly promotes the charge transfer activity. The i_0 values (>0.1 mA/mg) in ether electrolytes are much higher than those (0.02 to 0.03 mA/mg) in the carbonate one, further confirming the kinetic advantage of the former. In addition, the corresponding charge transfer resistance (R_{CT}) could be calculated by the following relationship

$$R_{CT} = \frac{RT}{F i_0}$$

The cells with ether electrolytes also enable the much lower R_{CT} values for both the intercalation and conversion regions. Note that the addition of TPFPB-LiF into the ether-based electrolyte is prone to boost the reconstruction of parent phase and consequent mass-charge transfer at high voltage, leading to a more decrease of R_{CT} value in the intercalation region compared with the TPFPB-free case. The introduction of solid-liquid F-transport mechanism probably improves the reversibility of F-rich structure conversion and then facilitates the sustainable redox reactions.

O ligand as an electron-conduction hinge in rutile phase is expected to upgrade the conversion kinetics. From the EIS comparison at different cycling stages (fig. S21), the $FeO_{0.7}F_{1.3}$ cell exhibits a decreased interface resistance (compared with the $FeO_{0.3}F_{1.7}$ cell) before cycling, in view of the reinforcement of charge transfer at a more conductive $FeO_{0.7}F_{1.3}$ interface. During the following cycles, the interface resistance values for $FeO_{0.7}F_{1.3}$ are still smaller than those for $FeO_{0.3}F_{1.7}$. Apart from the advantage of intrinsic conductivity, the less LiF precipitation for the former is also responsible for the R_i modification. From the pseudocapacitance analysis of $FeO_{0.7}F_{1.3}$ (fig. S22), its b values are lower for three main redox peaks compared with $FeO_{0.3}F_{1.7}$. The larger particle size for $FeO_{0.7}F_{1.3}$ and more sufficient bulk transport give rise to the relatively smaller capacitive contribution (around 66 to 79%) from 0.2 to 1.0 mV/s (*57*). The improvement of high-rate performance of $FeO_{0.7}F_{1.3}$ should root in the better electronic conductivity and crystallinity and then the favorable diffusion-controlled charge storage.

Reaction mechanism of $FeO_{0.3}F_{1.7}$

Previous researches suggest that the partial substitution of fluorine with oxygen in rutile FeF_2 modifies the ligand units and certainly complicates the phase evolution pathway including sequent intercalation-extrusion-conversion reactions (*15*, *16*). The intercalation reaction at high voltage occurs as the transition of initial mixed-anion rutile FeO_xF_{2-x} into a lithiated rutile-II phase of $Li_yFeO_xF_{2-x}$ ($y \leq x$). The phase-constant Li-ion solid solution process would enlarge unit cells with the reduction of Fe^{3+} to Fe^{2+}. When the Li content reaches (or is close to) the theoretically expected insertion stoichiometry, the rutile-II phase begins to transform into a rock salt phase with the extrusion of Fe and LiF. This process does not trigger the structural collapse of the cubic rock salt phase but rather a continuous separation of fluoride components from the intermediate Li—Fe—O—F phase until the termination in Li—Fe—O phase. Last, this rock salt phase converts to Fe and Li_2O at lower voltage via deeper lithiation reaction. Upon the subsequent charging, the reconstitution of the parent structure undergoes the divergent O/F delithiation pathways and is terminated in a mixture of O-rich rock salt and F-rich rutile phases. Owing to the restriction of thermodynamic and kinetic aspects, the partially recovered rutile phase is generally distorted and amorphous, and the rock salt phase grows into a secondary parent phase for the following cycling.

To understand the comprehensive conversion mechanism in a voltage range of 1.2 to 4.0 V, we study the phase and morphology of $FeO_{0.3}F_{1.7}$ cathode at terminal lithiated/delithiated states in the LiTFSI-LiF-TPFPB/DME system by TEM characterization (Fig. 5 and fig. S23). After $FeO_{0.3}F_{1.7}$ is discharged to 1.2 V, there are numerous dark-contrast nanoparticles uniformly embedded in light-contrast matrix (Fig. 5A), which is also indicated from the color contrast in dark-field image (Fig. 5C). From the magnified images (fig. S24), these nanodomains exhibit a square-like shape with a homogeneous size of ~10 nm, coinciding with the probable products of cubic rock salt, LiF, and Fe phases. The SAED pattern confirms the transformation

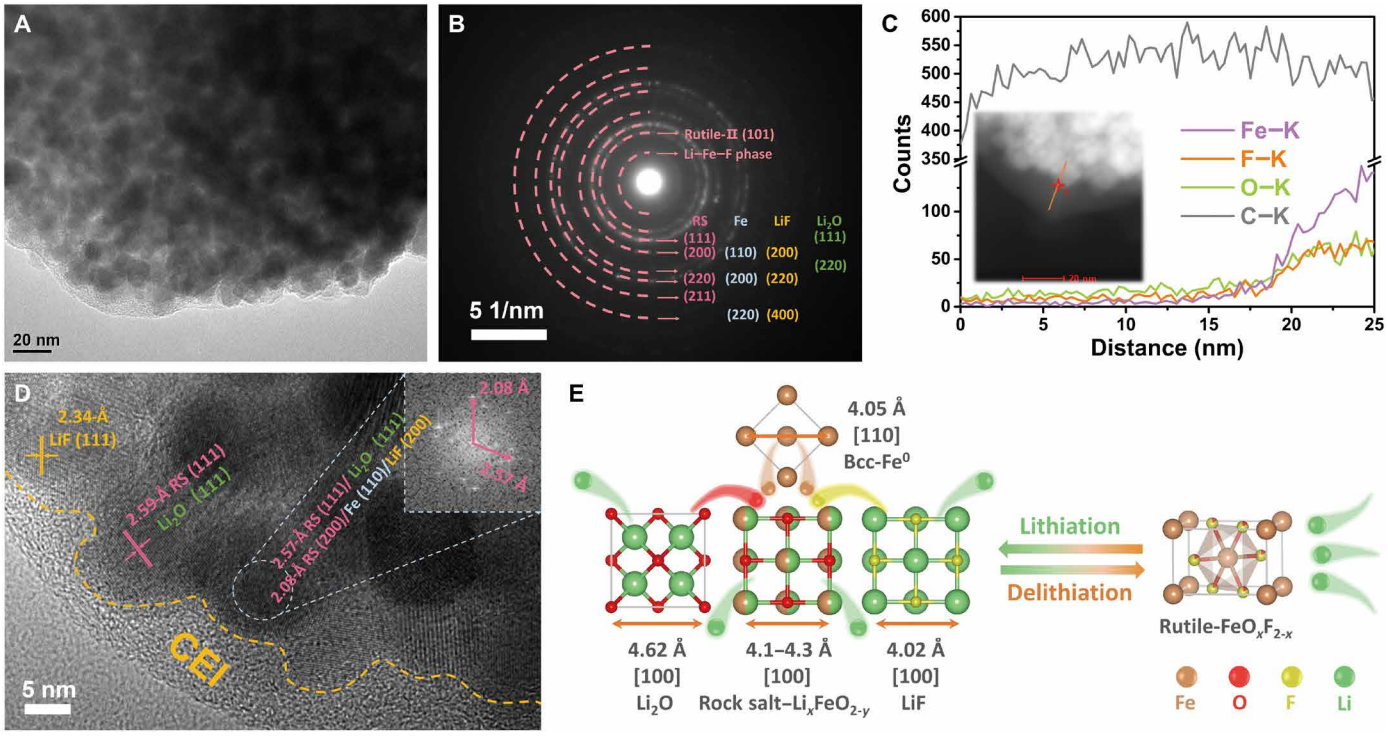

Fig. 5. Phase constitution and spatial distribution in lithiated $FeO_{0.3}F_{1.7}$ cathode. (**A** and **B**) TEM image and corresponding SAED pattern of electrode discharged to 1.2 V, showing dominant converted products of rock salt, metallic Fe, LiF, and Li_2O phases. (**C**) Line-scanning STEM-EDS analysis of a selected lithiated nanoparticle with CEI layer. Inset of (C): Dark-field image of nanodomain cluster with surface coating. (**D**) HRTEM image with observable lattice stripes corresponding to discharged products and with observable CEI layer on the nanodomain surface. Inset of (D): FFT pattern at the selected region, indicating a potential enrichment of multicubic phases including rock salt, Fe, LiF, and Li_2O. (**E**) Schematic of electrochemically driven structure transformation for rutile-type FeO_xF_{2-x} phase. The crystal structures of four lithiation-converted cubic phases have similar lattice constants.

from original rutile to these cubic structures (Fig. 5B) (*58*, *59*), including O-defected rock salt and extruded Li_2O phases via sufficient lithiation reaction. Besides, we occasionally find the reflection belonging to the maintained structure of rutile-II phase with relatively larger *d*-spacing. Another minor phase of HTB-type FeF_3 in cathode enables the prominent activation of conversion reaction under a cutoff voltage of 1.2 V, resulting in the major products of Fe and LiF phases (*35*). The smallest diffraction ring may be associated with a few undecomposed solid-solution Li—Fe—F phase with expanded lattice (*40*). According to the HRTEM image in Fig. 5D, the FFT pattern of the selected nanodomain with dark contrast reveals the (111) plane of rock salt/Li_2O phases, plus the characteristic lattice fringes with *d*-spacing of ~2.08 Å corresponding to a potential superposition of rock salt, Fe, and LiF reflections. The enrichment of multicubic phases with similar lattice constants is favorable for the reinjection of extruded Fe/F/O components into a rutile phase upon recharging (Fig. 5E). The undecomposed rock salt is prone to spatially hinder the boundary coarsening and grain aggregation/growth of active precipitation phases such as metallic Fe (*6*), and it is beneficial to local electron percolation. The rational distribution of converted products with cubic-on-cubic lattice coherence is in favor of the reconstitution of Fe—F(—O) phase during delithiation process (*16*). The bright diffraction rings in the SAED pattern and clear lattice fringes in HRTEM images reveal the high crystallinity of lithiated $FeO_{0.3}F_{1.7}$, which is correlated with the preserved conversion plateau and excellent cycling stability.

We also observe the conformal and continuous surface coating as CEI with a thickness of about 5 to 10 nm on these nanoparticles (Fig. 5D). In view of the poorly established CEI in the LiTFSI-DME system (*18*), the high-quality CEI in this case should stem from the self-decomposition of TPFPB or its knock-on effect on the derivations of other electrolyte components due to the strong Lewis acidity of TPFPB (*60*). This surface coating could effectively prevent the dissolution of active Fe/F-containing species and the side reaction of cathode-electrolyte interaction. Line-scanning STEM-EDS of lithiated cathode was carried out along the indicated line across an individual nanocrystal domain with CEI coating to disclose its composition distribution (Fig. 5C). As seen, prominent C and O signals with less fluctuation are detected in the region away from the nanodomain cluster, suggesting the CEI layer mainly comprising C and O with continuous and homogeneous distribution, which likely derive from ether chains. When scanning to the particle domain edge, the signals of corresponding elemental compositions get stronger together rapidly, and they show a similar variation tendency. The negligible Fe signal in only-CEI region indicates an effective suppression of Fe-based active species dissolution. There, the discernable F signal implies the presence of F doping in surface coating. The surface fluorination enables the potential enhancement of interfacial Li^+ permeability, as well as a robust CEI layer that reinforces the mechanical stability and endures the volume expansion of deep-lithiated fluoride (*30*).

For the delithiated state of $FeO_{0.3}F_{1.7}$ cathode after charging to 4.0 V, we observe numerous dark-contrast grains with larger size in

about 50 to 100 nm range (fig. S25A). The recovering of iron (oxy) fluoride is inevitably accompanied with boundary coarsening and grain growth. The combination reactions of multiple cubic conversion phases are responsible for the grain coarsening phenomenon. The optimization of F transfer kinetics by TPFPB additive likely facilitates the electrochemical synthesis of the F-rich rutile phase (e.g., FeO_xF_{2-x}, rutile FeF_2, or defect-trirutile FeF_3), according to the reappearance of characteristic (110) plane as indicated by the SAED pattern and HRTEM image (fig. S25, B and C). From the intensity contrast of concentric rings in SAED pattern, the O^{2-} anion seems to exhibit high mobility along another reconversion pathway, leading to the formation of O-rich rock salt with better structural ordering in the charged state. Incomplete reconstitution of origin rutile phase should account for the initial capacity loss. However, instead of the homogeneous doping in a single phase, the mixture of F-rich and O-rich phases with tight contact in nanoscale also enables the preservation of high-voltage plateaus and satisfactory cycling stability.

The chemical composition, particle size, and crystallinity are responsible for the evolution of electrode potential. As disclosed by work conducted in Maier's group (*61*), particle size and crystallinity are tightly associated with the thermodynamic behavior of electrode. Nanosized and amorphous effects contribute to excess surface energy and free enthalpy, which endow conversion electrode with higher reaction potential. During the repeated lithiation/delithiation, $FeO_{0.3}F_{1.7}$ inevitably undergoes electrochemical pulverization progress, resulting in the smaller nanodomains with weakened crystallinity (based on the TEM result). On the other hand, the stabilization of chemical composition also plays a crucial role in the preservation of raised plateaus. Benefiting from the facile F-transport channel, rutile/rock salt phases with high oxidation states could be reversibly reconstituted in the TPFPB-containing system (according to the TEM analysis of delithiated $FeO_{0.3}F_{1.7}$). Otherwise, the precipitation of insulating LiF tends to become inactivated because of its high dissociation energy. The dead LiF can impede the mass/charge transport between the surrounding active species. Insufficient extraction of Li^+ would reduce the Fe oxidation state at the charged stage, consequently causing the gradual degradation of discharge plateaus, as shown in the cases of conventional carbonate- and ether-based systems (fig. S8). Overall, the reconversion of highly fluorinated Fe-based constituents with nanosized/amorphized structures would contribute to the enhanced chemical potential of $FeO_{0.3}F_{1.7}$, corresponding to two distinct raised plateaus in the discharge curves with the progress of cycling.

Surface evolution of $FeO_{0.7}F_{1.3}$ in TPFPB-containing electrolyte

More evidences about the conversion mechanism and CEI evolution of FeO_xF_{2-x} can be collected from the XPS profiles of pristine and cycled cathodes in TPFPB-containing electrolyte (Fig. 6, fig. S26, and table S5). After discharging to 1.2 V, the peaks in Fe $2p_{3/2}$ shift to the positions of lower binding energies with the formation of dominant rock salt Li—Fe—O—F phase (at 709.9 eV) and minor Fe^0 and Li—Fe—F phases (respectively at 707.2 and 712.9 eV) (*33*, *62*, *63*). There, a lower Fe oxidation state in rock salt phase is close to 2+ in the terminal F-extrusion phase of Li—Fe—O. These lithiated Fe species are also found in Fe 3p at corresponding positions. In the same spectrum, a strong Li 1s peak emerges at 56.0 eV belonging to LiF, and accordingly, the positive displacement of F 1s peak is observed (fig. S26A) (*45*). Meanwhile, the Fe—O signal is weakened in O 1s, and a new signal corresponding to Li_2O generates at 528.5 eV (*64*). The Li_2O signal is also detectable at 53.9 eV in Li 1s. These results suggest the breakage of Fe—F and Fe—O bonds in parent phase and simultaneous precipitation of metallic Fe, LiF, and Li_2O phases during deep lithiation. The appearance of weakened Fe^0 peak is ascribed to the screening effect in view of the formation of the robust CEI layer. The reduced components on electrode surface are easily oxidized when exposed in air during sample transfer. It would also affect the peak intensity of Fe^0 because of the surface sensitivity of XPS technology. When recharged to 4.0 V, the electrode displays a regeneration of rutile peak and the positive displacement of rock salt peak with the concomitant dilution of metallic Fe peak in Fe $2p_{3/2}$ (Fig. 6A). The decrease of Li—F and Li—O signals (in Li 1s and O 1s) in exchange for the intensification of Fe—F and Fe—O signals is indicative of the electrochemical synthesis of F-rich rutile/defect trirutile FeF_3 and O-rich rock salt during Li extraction (Fig. 6B and fig. S26B). The residual LiF may be the "dead mass" accumulated in early cycles but could be gradually reactivated by F receptor with the progress of repeated conversion reaction, corresponding to the appearance of capacity-boosting period in long-term cycling. Overall, the local bonding evolution of active components for $FeO_{0.7}F_{1.3}$ is in agreement with the phase analysis of TEM during (de)lithiation. The doping of higher-content lattice-O in rutile-type fluoride would decrease the extrusion of F components and increase the fraction of rock salt phase at discharged state. This effect is kinetically favorable for the reversible structural transition upon charging. This is a critical reason for the achievement of superior cycling stability and rate capability via fluoride genetic manipulation.

The C 1s spectra explain the main chemical nature of surface composition formed on the cycled electrode (Fig. 6C). The polyvinylidene fluoride (PVDF) binder should contribute to appearance of C—F peak at 290.0 eV in C 1s after discharging (*41*). The rise of C—O and C═O peaks may originate from the DME-derivative species on the cathode surface (*20*). We also observe that the already existed C—N peak appears to have an intensity enhancement during cycling, which possibly results from the decomposition of imide-based anion. In this process, the CEI is prone to be increasingly functionalized with fluorine and sulfur as well (fig. S26C). Upon charge, a deeper S doping with S—F and S═O bonds strengthens the corresponding peaks at 687.8 eV in F 1s and 532.2 eV in O 1s (*20*). Note that the F signal in C 1s shifts to a higher binding energy probably as a consequence of the enhanced fluorination degree of CF_x moieties by fluorine incorporation from F-rich Li salt or additive (*65*). This fluorination characteristic is beneficial for electroactive and mechanical properties. In addition, the surface coating is further oxidized and nitrided with increased contents of oxygen and nitrogen bound to carbon at high voltage (fig. S26D). The potential catalysis of the reduced transition metal on the decomposition of electrolyte component cannot be ruled out (*66*). The minor shoulder peak around 282.6 eV in C 1s emerges after cycling and is assigned to Li_xC (*64*), which may stem from the lithiation of carbon matrix or few detained Li^+ in the CEI layer. During cycling, the CEI layer performs some dynamical redox behaviors before stabilization, but it does not compromise both the capacity and CE performance of cathode.

To mitigate the influences from signal screening by surface coating and air contamination especially to the reduced active species, the XPS depth profiling with continuous ion beam etching was carried out for the discharged $FeO_{0.7}F_{1.3}$ electrode to further confirm its lithiated products (fig. S27). During etching, the overall shape of spectra does not change apparently, ensuring the reliability of the abovementioned XPS analysis about conversion mechanism. In

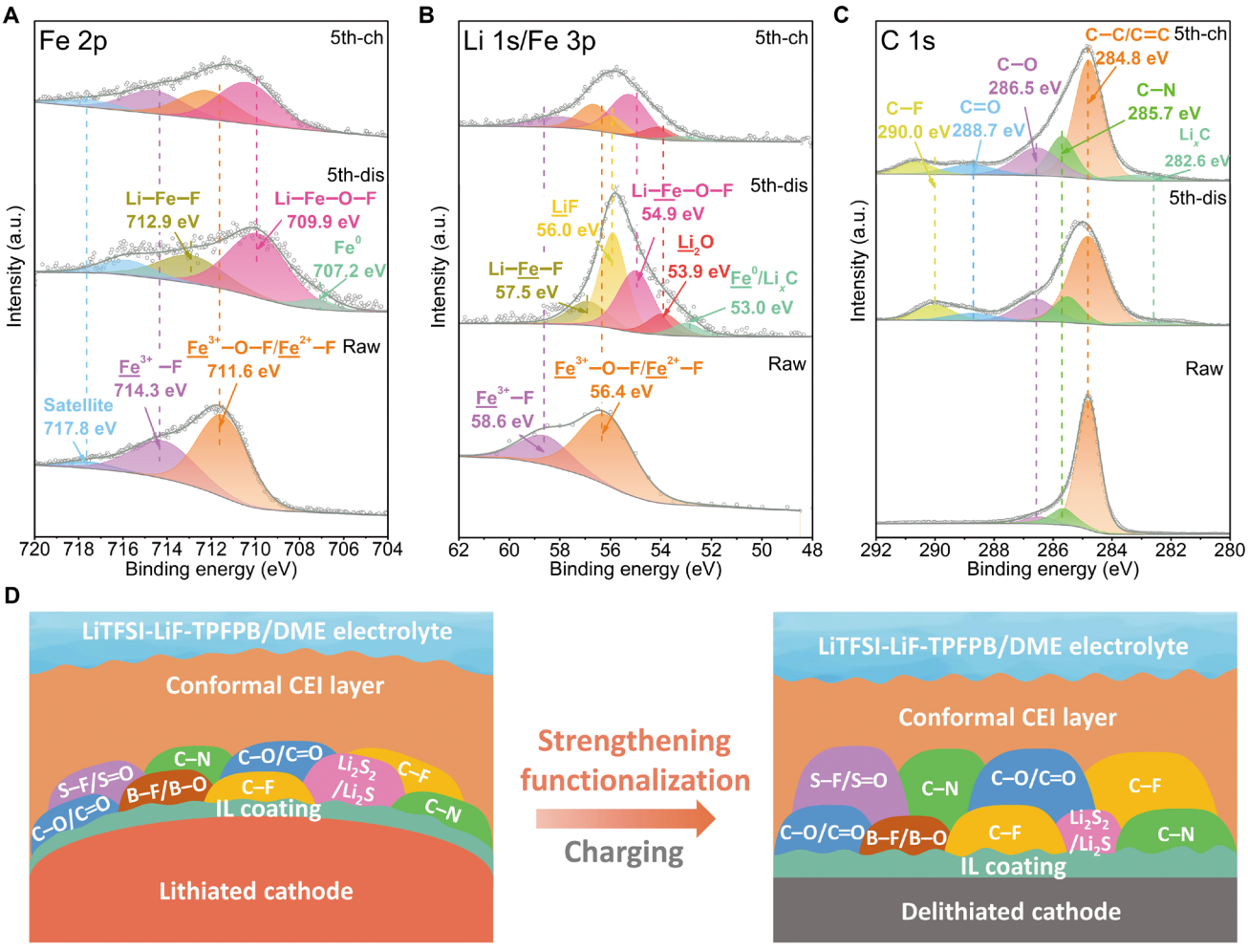

Fig. 6. Surface evolution of cycled $FeO_{0.7}F_{1.3}$ in TPFPB-containing electrolyte. XPS of (**A**) Fe $2p_{3/2}$, (**B**) Li 1s/Fe 3p, and (**C**) C 1s for pristine, discharged (dis), and charged (ch) electrodes. (**D**) Schematic illustration of the conformal CEI layer with various functional moieties on the cathode surface derived from the LiTFSI-LiF-TPFPB/DME electrolyte.

view of the weakening of signals by CEI coating, the peaks related to active elements gradually become more pronounced with the progress of etching especially for those of converted phases (e.g., Fe^0, LiF, and Li_2O). Accordingly, an apparent displacement toward the higher binding energy of M-F peak in F 1s is observed. The shoulder peak around 683 eV in F 1s vanishes completely after etching only for 20 s, suggesting that it should be associated with contaminant. The S-containing products from electrolyte decomposition consist of S—F/S═O species and Li_2S_2/Li_2S (*20*, *67*). Their opposite concentration evolutions from surface to subsurface imply the different accumulation regions for them. Different from the stable signals for most C-containing CEI components, the C—N peak (or N 1s signal) is intensified with the thinning of the CEI layer and when approaching to the retained IL coating on fluoride particle. This residual IL serves as an organic substrate for the deposition of the electrolyte-derivative CEI layer. With the surface elimination, the B—F and B—O components are detected from B 1s, and they may further strengthen the CEI layer with functions of suppressing cation dissolution and holding particle integrity (*19*, *68*). The moderate B signal, even indiscernible before etching, indicates that TPFPB only partially contributes to the protective CEI construction without continuous decomposition. As shown in Fig. 6D, the XPS analysis indicates the homogeneity of TPFPB-LiF–modulated CEI in different depth, which is in favor of the improvement of CEI toughness and, therefore, the spatial confinement and mechanical stress adjustment of electrochemical conversion products (*23*).

DISCUSSION

In summary, we design a solid-liquid fluorine channel to activate the highly reversible conversion reaction of iron oxyfluoride cathodes in the TPFPB-containing ether electrolyte. The boron-based receptor with F solvation function facilitates the LiF splitting and rebonding with Fe species via a facile F-transport channel to bypass the tough solid-solid conversion. The in situ formation of the conformal and functionalized CEI layer is favorable for the chemomechanical stability of cathode (e.g., spatial confinement and mechanical stress adjustment) and consequently sustaining electroactive behavior. The rutile-type fluorides with homogeneous mixed anions are synthesized via self–oxygen penetration process, and they perform a reliable phase

evolution pathway by introducing a stable second-generation parent phase of rock salt, which has high lattice coherency with extruded phases of Fe, LiF, and Li_2O. Benefiting from the construction of facile round-trip F/Li-transport pathways and favorable CEI layer, $FeO_{0.3}F_{1.7}$ and $FeO_{0.7}F_{1.3}$ cathodes enable the sustaining conversion reaction with energy efficiency approaching 80%, high capacity retention of 472 and 484 mAh/g after 100 cycles at 100 mA/g, and superior rate capability with reversible capacities of 271 and 320 mAh/g at 2 A/g. Their energy densities are achieved at 1100 Wh/kg for $FeO_{0.3}F_{1.7}$ and 700 Wh/kg for $FeO_{0.7}F_{1.3}$ under the power densities of 220 and 4300 W/kg, respectively. The key finding of solid-liquid fluorine channel may provide an effective strategy to develop fluorine-conversion battery systems with high energy density.

MATERIALS AND METHODS

Synthesis of iron oxyfluorides

For the fabrication of $FeO_{0.3}F_{1.7}$ and $FeO_{0.7}F_{1.3}$, a hydrated iron fluoride serves as the precursor, and it was synthesized by a typical dissolution-precipitation method based on IL ambience of 1-butyl-3-methylimidazolium tetrafluoroborate with $Fe(NO_3)_3{\cdot}9H_2O$ (Aladdin, 98%) as the iron source, according to our previous work (*26*). To improve the electronic conductivity of fluoride, an accurate amount of KB (25 weight %) was added into IL to form a $FeF_3{\cdot}3H_2O$/KB composite. Last, the $FeO_{0.3}F_{1.7}$ and $FeO_{0.7}F_{1.3}$ samples were obtained by annealing $FeF_3{\cdot}3H_2O$/KB under N_2 flow in a tube furnace at 300°C for 2 and 5 hours (with a heating rate of 5°C/min), respectively.

Electrolyte preparation

LiTFSI, DOL, DME, EC, and DMC were obtained from Sigma-Aldrich. $LiPF_6$ was provided by Alfa Aesar. LiF was purchased from Aladdin. TPFPB was acquired from Tokyo Chemical Industry Co. Ltd. All reagents for preparing electrolytes were of analytical grade without further purification and were kept in an argon-filled glove box (<0.1 ppm for water and oxygen).

Three kinds of electrolytes were selected for fluoride electrochemical performance comparison. The optimized LiTFSI-LiF-TPFPB/DME electrolyte was prepared by adding a mixture of 1 M LiTFSI, 0.5 M LiF, and 0.05 M TPFPB into the DME followed by vigorous magnetic stirring for 24 hours. A clear solution was obtained after filtering the undissolved LiF powder. The optimization of TPFPB-containing electrolytes was carried out by adjusting the concentration of LiF and TFPPB. The reference ether-based electrolyte consists of 1 M LiTFSI dissolved in DOL and DME (1:1, v/v). The conventional carbonate-based electrolyte contains 1 M $LiPF_6$ dissolved in EC and DMC (1:1, v/v).

Electrochemical measurement

The electrochemical performance is characterized by using CR2025-type coin cells of two-electrode configuration, including iron oxyfluoride ($FeO_{0.3}F_{1.7}$ or $FeO_{0.7}F_{1.3}$) as working electrode and high-purity lithium foil as counter electrode. The working electrode was prepared by mixing as-synthesized oxyfluoride powder, super P, and PVDF (which is uniformly dissolved in 1-methyl-2-pyrrolidinone) with a weight ratio of 8:1:1. The mixture was then manually ground into a homogeneous slurry and pasted onto pure aluminum foil via doctor blade, followed by drying in a vacuum oven at 80°C for 20 hours before it was punched into circular electrode sheets. Celgard 2400 was used as the separator. The whole cell assembly process was conducted in an Ar-filled glove box. The volume of electrolyte injected in each coin cell is controlled at about 25 μl by pipette.

The galvanostatic charge-discharge measurement was performed at room temperature under different current densities from 100 to 2 A/g in a voltage range of 1.2 to 4.0 V on the Land multichannel battery testing system (CT2001A). Impedance measurement of pristine and cycled cells was done by using a Solartron frequency analyzer (1260–1296) in a frequency range from 100 kHz to 0.1 Hz. CV and Tafel analysis were performed on an electrochemical workstation (VersaSTAT 3, AMETEK Scientific Instruments). CV measurement of fluoride-based cells was run in a voltage range from 1.2 to 4.0 V at different scan rates from 0.1 to 1.0 mV/s. Single-cycle CV for evaluating electrolyte stability was measured at a scan rate of 2.0 mV/s in the architecture of coin cell with Al foil as the working electrode and Li foil as the counter electrode. Tafel analysis was performed during the 10th discharge process by holding the voltage at either intercalation plateau or conversion plateau (e.g., either 3.05 or 2.03 V in the case of TPFPB-based $FeO_{0.3}F_{1.7}$ cell) for 1 hour followed by a linear scan at 1 mV/s with the voltage range of ±200 mV around the open-circuit voltage. The holding potential should be slightly adjusted on the basis of the variation of plateau position in different electrolyte systems. GITT was operated at a low current density of 35 mA/g for 1 hour followed by open-circuit relaxation for 6 hours to allow the system to reach a (quasi-)equilibrium state.

Material characterization

Crystal structure and crystallinity of both oxyfluoride samples were analyzed using XRD (D8 DISCOVER, Bruker) with Cu Kα radiation in a 2θ range of 10° to 80° at a scan rate of 10°/min. The Rietveld refinement on the diffraction pattern was conducted by the General Structure Analysis System II (GSAS-II) software to determine the oxygen content x in FeO_xF_{2-x} and molar ratio of components. The SEM images were acquired from a FEI Magellan 400. The bright/dark-field TEM images and SAED patterns were collected from a transmission electron microscope (JEOL JSM-6700F; operated at 200 kV), which is equipped with the HAADF-STEM model, to disclose the morphology/microstructure information and element distribution of pristine and cycled electrodes. XPS (ESCAlab-250) with an Al anode source was carried out to detect the (sub)surface composition and bonding situation of pristine and cycled electrodes. TGA was performed on TA Instruments SDT Q600 under oxygen flow with a heating rate of 10°C/min from room temperature to 800°C. For ex situ characterization, the cycled cells at various discharge and charge stages were transferred into an Ar-filled glove box and disassembled immediately for taking out the working electrodes. Subsequently, the collected electrodes were rinsed several times with the corresponding solvent of original electrolyte to ensure the removal of residual salts. They were then dried under argon overnight before further analysis.

For the characterization of TPFPB with F solvation function, the LiF/DME, TPFPB-LiF/DME, and TPFPB/DME solutions were prepared by adding 0.5 M LiF, 0.5 M LiF with 0.05 M TPFPB, and 0.05 M TPFPB into DME, respectively, followed by vigorous magnetic stirring for 24 hours. The LiF-containing solutions were obtained after filtering the undissolved LiF powder. To evaluate the promoting effect of TFPPB on LiF dissociation, the Li^+ concentration in the LiF/DME and TPFPB-LiF/DME solutions were analyzed by ICP-OES (Agilent 725). To confirm the coordination between anion acceptor and fluorine ion, TPFPB-LiF/DME and TPFPB/DME solutions were used for NMR spectroscopy and FTIR spectroscopy measurements. The

^{19}F NMR spectra were collected on a Bruker Avance III HD 400 MHz spectrometer. FTIR spectroscopy was carried out by Nicolet iS10 in the range of 4000 to 400 cm^{-1}. To further evaluate the electrochemical stability of the F-transport channel during cycling, we performed the ^{19}F NMR measurement on the pristine and cycled LiTFSI-LiF-TPFPB/DME electrolytes. For collecting the cycled electrolyte, the separator with adsorbed electrolyte was taken out from the cycled cell and was immersed in the original solvent.

Computational details

DFT calculations were performed by using the Vienna *Ab initio* Simulation Package (VASP). The projector-augmented wave pseudopotentials were adopted as implemented in VASP and Perdew-Burke-Ernzerhof parametrization of the generalized gradient approximation (GGA) that was used for the exchange-correlation functional. We performed the computations with a cutoff energy of 500 eV. The structures are relaxed until the energy variation is less than 10^{-5} eV. The force convergence criteria for binding/dissociation energies and reaction activation energy are set as 0.03 and 0.08 eV/Å, respectively. The binding energy (E_b) between TPFPB and F is described as $E_b = E_{F+TPFPB} - (E_F + E_{TPFPB})$. The dissociation energies (E_d) for LiF without and with TPFPB are defined as $E_d = E_F + E_{Li} - E_{LiF}$ and $E_d = E_{F+TPFPB} + E_{Li} - (E_{LiF} + E_{TPFPB})$, respectively, where E_{LiF} is the total energy of the LiF crystal; E_{Li}, E_F, and E_{TPFPB} are the energies of the free Li, F, and TPFPB molecules, respectively; and $E_{F+TPFPB}$ is the total energy of TPFPB molecule with one F atom attached. The activation barrier and potential F-transport pathway of LiF—Fe system were estimated by the CI-NEB method. To simplify the calculation models, the F atom breaks away from the initial Li—F state and is finally bonded with Fe atom. When the TPFPB molecule participates in the LiF—Fe system, the F atom would preferentially attach to TPFPB first and then combines with the Fe atom. The strong correlation of the d orbital in Fe atoms was addressed with a U_{eff} value of 5.3 eV using the GGA + U method. The ESP-mapped molecular surfaces of TPFPB molecule and TPFPB-F complex were obtained using Multiwfn3.8 and Visual Molecular Dynamics (VMD) program, based on single-point energy calculations conducted by Gaussian package at the B3LYP/6-31G(d) level.

SUPPLEMENTARY MATERIALS

Supplementary material for this article is available at https://science.org/doi/10.1126/sciadv.abj1491

REFERENCES AND NOTES

1. Z. P. Cano, D. Banham, S. Y. Ye, A. Hintennach, J. Lu, M. Fowler, Z. Chen, Batteries and fuel cells for emerging electric vehicle markets. *Nat. Energy* **3**, 279–289 (2018).
2. L. Wang, Z. Wu, J. Zou, P. Gao, X. Niu, H. Li, L. Chen, Li-free cathode materials for high energy density lithium batteries. *Joule* **3**, 2086–2102 (2019).
3. F. Wu, G. Yushin, Conversion cathodes for rechargeable lithium and lithium-ion batteries. *Energ. Environ. Sci.* **10**, 435–459 (2017).
4. P. G. Bruce, S. A. Freunberger, L. J. Hardwick, J.-M. Tarascon, Li-O_2 and Li-S batteries with high energy storage. *Nat. Mater.* **11**, 19–29 (2012).
5. C. Li, K. Chen, X. Zhou, J. Maier, Electrochemically driven conversion reaction in fluoride electrodes for energy storage devices. *npj Comput. Mater.* **4**, 22 (2018).
6. F. Wang, R. Robert, N. A. Chernova, N. Pereira, F. Omenya, F. Badway, X. Hua, M. Ruotolo, R. Zhang, L. J. Wu, V. Volkov, D. Su, B. Key, M. S. Whittingham, C. P. Grey, G. G. Amatucci, Y. M. Zhu, J. Graetz, Conversion reaction mechanisms in lithium ion batteries: Study of the binary metal fluoride electrodes. *J. Am. Chem. Soc.* **133**, 18828–18836 (2011).
7. L. Li, R. Jacobs, P. Gao, L. Gan, F. Wang, D. Morgan, S. Jin, Origins of large voltage hysteresis in high-energy-density metal fluoride lithium-ion battery conversion electrodes. *J. Am. Chem. Soc.* **138**, 2838–2848 (2016).
8. H. Arai, S. Okada, Y. Sakurai, J.-i. Yamaki, Cathode performance and voltage estimation of metal trihalides. *J. Power Sources* **68**, 716–719 (1997).
9. D. Cao, C. Yin, D. Shi, Z. Fu, J. Zhang, C. Li, Cubic perovskite fluoride as open framework cathode for Na-ion batteries. *Adv. Funct. Mater.* **27**, 1701130 (2017).
10. C. Li, C. Yin, L. Gu, R. Dinnebier, X. Mu, P. A. van Aken, J. Maier, An $FeF_3{\cdot}0.5H_2O$ polytype: A microporous framework compound with intersecting tunnels for Li and Na batteries. *J. Am. Chem. Soc.* **135**, 11425–11428 (2013).
11. F. Wu, V. Srot, S. Chen, S. Lorger, P. A. van Aken, J. Maier, Y. Yu, 3D honeycomb architecture enables a high-rate and long-life iron (III) fluoride–lithium battery. *Adv. Mater.* **31**, 1905146 (2019).
12. S. W. Kim, D. H. Seo, H. Gwon, J. Kim, K. Kang, Fabrication of FeF_3 nanoflowers on CNT branches and their application to high power lithium rechargeable batteries. *Adv. Mater.* **22**, 5260–5264 (2010).
13. N. Pereira, F. Badway, M. Wartelsky, S. Gunn, G. G. Amatucci, Iron oxyfluorides as high capacity cathode materials for lithium batteries. *J. Electrochem. Soc.* **156**, A407–A416 (2009).
14. M. Burbano, M. Duttine, B. J. Morgan, O. J. Borkiewicz, K. W. Chapman, A. Wattiaux, A. Demourgues, H. Groult, M. Salanne, D. Dambournet, Impact of anion vacancies on the local and electronic structures of iron-based oxyfluoride electrodes. *J. Phys. Chem. Lett.* **10**, 107–112 (2019).
15. K. M. Wiaderek, O. J. Borkiewicz, E. Castillo-Martínez, R. Robert, N. Pereira, G. G. Amatucci, C. P. Grey, P. J. Chupas, K. W. Chapman, Comprehensive insights into the structural and chemical changes in mixed-anion FeOF electrodes by using operando PDF and NMR spectroscopy. *J. Am. Chem. Soc.* **135**, 4070–4078 (2013).
16. X. Fan, E. Hu, X. Ji, Y. Zhu, F. Han, S. Hwang, J. Liu, S. Bak, Z. Ma, T. Gao, S.-C. Liou, J. Bai, X.-Q. Yang, Y. Mo, K. Xu, D. Su, C. Wang, High energy-density and reversibility of iron fluoride cathode enabled via an intercalation-extrusion reaction. *Nat. Commun.* **9**, 2324 (2018).
17. X. Fan, C. Luo, J. Lamb, Y. Zhu, K. Xu, C. Wang, PEDOT encapsulated FeOF nanorod cathodes for high energy lithium-ion batteries. *Nano Lett.* **15**, 7650–7656 (2015).
18. Q. Huang, K. Turcheniuk, X. Ren, A. Magasinski, D. Gordon, N. Bensalah, G. Yushin, Insights into the effects of electrolyte composition on the performance and stability of FeF_2 conversion-type cathodes. *Adv. Energy Mater.* **9**, 1803323 (2019).
19. E. B. Zhao, O. Borodin, X. Gao, D. Lei, Y. Xiao, X. Ren, W. Fu, A. Magasinski, K. Turcheniuk, G. Yushin, Lithium-iron (III) fluoride battery with double surface protection. *Adv. Energy Mater.* **8**, 1800721 (2018).
20. W. Gu, O. Borodin, B. Zdyrko, H.-T. Lin, H. Kim, N. Nitta, J. Huang, A. Magasinski, Z. Milicev, G. Berdichevsky, G. Yushin, Lithium-iron fluoride battery with in situ surface protection. *Adv. Funct. Mater.* **26**, 1507–1516 (2016).
21. W. Fu, E. Zhao, Z. Sun, X. Ren, A. Magasinski, G. Yushin, Iron fluoride-carbon nanocomposite nanofibers as free-standing cathodes for high-energy lithium batteries. *Adv. Funct. Mater.* **28**, 1801711 (2018).
22. O. Borodin, J. Self, K. A. Persson, C. Wang, K. Xu, Uncharted waters: Super-concentrated electrolytes. *Joule* **4**, 69–100 (2020).
23. Q. Huang, K. Turcheniuk, X. Ren, A. Magasinski, A.-Y. Song, Y. Xiao, D. Kim, G. Yushin, Cycle stability of conversion-type iron fluoride lithium battery cathode at elevated temperatures in polymer electrolyte composites. *Nat. Mater.* **18**, 1343–1349 (2019).
24. Y. Zhang, J. Meng, K. Chen, H. Wu, J. Hu, C. Li, Garnet-based solid-state lithium fluoride conversion batteries benefiting from eutectic interlayer of superior wettability. *ACS Energy Lett.* **5**, 1167–1176 (2020).
25. K. Kumagae, K.-i. Okazaki, K. Matsui, H. Horino, T. Hirai, J.-i. Yamaki, Z. Ogumi, Improvement of cycling performance of FeF_3-based lithium-ion battery by boron-based additives. *J. Electrochem. Soc.* **163**, A1633–A1636 (2016).
26. C. Li, L. Gu, J. W. Tong, J. Maier, Carbon nanotube wiring of electrodes for high-rate lithium batteries using an imidazolium-based ionic liquid precursor as dispersant and binder: A case study on iron fluoride nanoparticles. *ACS Nano* **5**, 2930–2938 (2011).
27. C. Li, X. Mu, P. A. van Aken, J. Maier, A high-capacity cathode for lithium batteries consisting of porous microspheres of highly amorphized iron fluoride densified from its open parent phase. *Adv. Energy Mater.* **3**, 113–119 (2013).
28. M. Burbano, M. Duttine, O. Borkiewicz, A. Wattiaux, A. Demourgues, M. Salanne, H. Groult, D. Dambournet, Anionic ordering and thermal properties of $FeF_3{\cdot}3H_2O$. *Inorg. Chem.* **54**, 9619–9625 (2015).
29. F. J. Brink, R. L. Withers, L. Norén, Nonstoichiometric, rutile-type, solid solutions in the $Fe^{II}F_2$–$Fe^{III}OF$ system. *J. Solid State Chem.* **161**, 31–37 (2001).
30. K. Chen, Y. Zhang, C. Li, High-rate nanostructured pyrite cathodes enabled by fluorinated surface and compact grain stacking via sulfuration of ionic liquid coated fluorides. *ACS Nano* **12**, 12444–12455 (2018).
31. M. V. Koudriachova, N. M. Harrison, S. W. de Leeuw, Diffusion of Li-ions in rutile. An ab initio study. *Solid State Ion.* **157**, 35–38 (2003).
32. I. D. Gocheva, I. Tanaka, T. Doi, S. Okada, J.-i. Yamaki, A new iron oxyfluoride cathode active material for Li-ion battery, Fe_2OF_4. *Electrochem. Commun.* **11**, 1583–1585 (2009).

33. A. P. Grosvenor, B. A. Kobe, M. C. Biesinger, N. S. McIntyre, Investigation of multiplet splitting of Fe 2p XPS spectra and bonding in iron compounds. *Surf. Interface Anal.* **36**, 1564–1574 (2004).
34. G. Bhargava, I. Gouzman, C. M. Chun, T. A. Ramanarayanan, S. L. Bernasek, Characterization of the "native" surface thin film on pure polycrystalline iron: A high resolution XPS and TEM study. *Appl. Surf. Sci.* **253**, 4322–4329 (2007).
35. J. Hu, Y. Zhang, D. Cao, C. Li, Dehydrating bronze iron fluoride as a high capacity conversion cathode for lithium batteries. *J. Mater. Chem. A* **4**, 16166–16174 (2016).
36. H. Inoue, K. Hosoya, N. Kannari, J.-I. Ozaki, Influence of heat-treatment of ketjen black on the oxygen reduction reaction of Pt/C catalysts. *J. Power Sources* **220**, 173–179 (2012).
37. X. Zhou, H. Yang, F. Wang, [BMIM]BF_4 ionic liquids as effective inhibitor for carbon steel in alkaline chloride solution. *Electrochim. Acta* **56**, 4268–4275 (2011).
38. C. Liu, Y. Yang, C. Zhang, S. Wu, L. Wei, F. Guo, G. M. Arumugam, J. Hu, X. Liu, J. Lin, R. E. I. Schropp, Y. Mai, Tailoring C_{60} for efficient inorganic $CsPbI_2Br$ perovskite solar cells and modules. *Adv. Mater.* **32**, 1907361 (2020).
39. G. Henkelman, B. P. Uberuaga, H. Jónsson, A climbing image nudged elastic band method for finding saddle points and minimum energy paths. *J. Chem. Phys.* **113**, 9901–9904 (2000).
40. L. Liu, H. Guo, M. Zhou, Q. Wei, Z. Yang, H. Shu, X. Yang, J. Tan, Z. Yan, X. Wang, A comparison among $FeF_3{\cdot}3H_2O$, $FeF_3{\cdot}0.33H_2O$ and FeF_3 cathode materials for lithium ion batteries: Structural, electrochemical, and mechanism studies. *J. Power Sources* **238**, 501–515 (2013).
41. A. W. Xiao, H. J. Lee, I. Capone, A. Robertson, T.-U. Wi, J. Fawdon, S. Wheeler, H.-W. Lee, N. Grobert, M. Pasta, Understanding the conversion mechanism and performance of monodisperse FeF_2 nanocrystal cathodes. *Nat. Mater.* **19**, 644–654 (2020).
42. V. Etacheri, R. Marom, R. Elazari, G. Salitra, D. Aurbach, Challenges in the development of advanced Li-ion batteries: A review. *Energ. Environ. Sci.* **4**, 3243–3262 (2011).
43. W. Xu, J. Xiao, D. Wang, J. Zhang, J.-G. Zhang, Effects of nonaqueous electrolytes on the performance of lithium/air batteries. *J. Electrochem. Soc.* **157**, A219–A224 (2010).
44. J. K. Ko, K. M. Wiaderek, N. Pereira, T. L. Kinnibrugh, J. R. Kim, P. J. Chupas, K. W. Chapman, G. G. Amatucci, Transport, phase reactions, and hysteresis of iron fluoride and oxyfluoride conversion electrode materials for lithium batteries. *ACS Appl. Mater. Interfaces* **6**, 10858–10869 (2014).
45. Y. Zhao, K. Wei, H. Wu, S. Ma, J. Li, Y. Cui, Z. Dong, Y. Cui, C. Li, LiF splitting catalyzed by dual metal nanodomains for an efficient fluoride conversion cathode. *ACS Nano* **13**, 2490–2500 (2019).
46. Y. Yamashita, M. Okada, K. Suyama, H. Kasahara, Equilibrium polymerization of 1.3-dioxolane. *Makromol. Chem.* **114**, 146–154 (1968).
47. V. Gutmann, Empirical parameters for donor and acceptor properties of solvents. *Electrochim. Acta* **21**, 661–670 (1976).
48. Q. F. Zheng, Y. Yamada, R. Shang, S. Ko, Y.-Y. Lee, K. Kim, E. Nakamura, A. Yamada, A cyclic phosphate-based battery electrolyte for high voltage and safe operation. *Nat. Energy* **5**, 291–298 (2020).
49. C. L. Li, Z. W. Fu, Electrochemical characterization of amorphous $LiFe(WO_4)_2$ thin films as positive electrodes for rechargeable lithium batteries. *Electrochim. Acta* **53**, 6434–6443 (2008).
50. V. Augustyn, J. Come, M. A. Lowe, J. W. Kim, P.-L. Taberna, S. H. Tolbert, H. D. Abruña, P. Simon, B. Dunn, High-rate electrochemical energy storage through Li^+ intercalation pseudocapacitance. *Nat. Mater.* **12**, 518–522 (2013).
51. A. J. Bard, L. R. Faulkner, *Electrochemical Methods: Fundamentals and Applications* (Wiley, ed. 2, 2001).
52. V. Murugesan, J. S. Cho, N. Govind, A. Andersen, M. J. Olszta, K. S. Han, G. Li, H. Lee, D. M. Reed, V. L. Sprenkle, S. Cho, S. K. Nune, D. Choi, Lithium insertion mechanism in iron fluoride nanoparticles prepared by catalytic decomposition of fluoropolymer. *ACS Appl. Energy Mater.* **2**, 1832–1843 (2019).
53. S.-K. Jung, H. Kim, M. G. Cho, S.-P. Cho, B. Lee, H. Kim, Y.-U. Park, J. Hong, K.-Y. Park, G. Yoon, W. M. Seong, Y. Cho, M. H. Oh, H. Kim, H. Gwon, I. Hwang, T. Hyeon, W.-S. Yoon, K. Kang, Lithium-free transition metal monoxides for positive electrodes in lithium-ion batteries. *Nat. Energy* **2**, 16208 (2017).
54. X. Hua, A. S. Eggeman, E. Castillo-Martínez, R. Robert, H. S. Geddes, Z. Lu, C. J. Pickard, W. Meng, K. M. Wiaderek, N. Pereira, G. G. Amatucci, P. A. Midgley, K. W. Chapman, U. Steiner, A. L. Goodwin, C. P. Grey, Revisiting metal fluorides as lithium-ion battery cathodes. *Nat. Mater.* **20**, 841–850 (2021).
55. C. J. Wen, B. Boukamp, R. A. Huggins, W. Weppner, Thermodynamic and mass transport properties of "LiAl". *J. Electrochem. Soc.* **126**, 2258–2266 (1979).
56. J. M. Whiteley, S. Hafner, S. S. Han, S. C. Kim, K. H. Oh, S. H. Lee, FeS_2-imbedded mixed conducting matrix as a solid battery cathode. *Adv. Energy Mater.* **6**, 1600495 (2016).
57. T. Brezesinski, J. Wang, S. H. Tolbert, B. Dunn, Ordered mesoporous α-MoO_3 with iso-oriented nanocrystalline walls for thin-film pseudocapacitors. *Nat. Mater.* **9**, 146–151 (2010).
58. M. Sina, K.-W. Nam, D. Su, N. Pereira, X.-Q. Yang, G. G. Amatucci, F. Cosandey, Structural phase transformation and Fe valence evolution in FeO_xF_{2-x}/C nanocomposite electrodes during lithiation and de-lithiation processes. *J. Mater. Chem. A* **1**, 11629–11640 (2013).
59. S.-W. Kim, N. Pereira, N. A. Chernova, F. Omenya, P. Gao, M. S. Whittingham, G. G. Amatucci, D. Su, F. Wang, Structure stabilization by mixed anions in oxyfluoride cathodes for high-energy lithium batteries. *ACS Nano* **9**, 10076–10084 (2015).
60. Q. Wang, D. Zheng, M. E. McKinnon, X.-Q. Yang, D. Qu, Kinetic investigation of catalytic disproportionation of superoxide ions in the non-aqueous electrolyte used in Li-air batteries. *J. Power Sources* **274**, 1005–1008 (2015).
61. O. Delmer, P. Balaya, L. Kienle, J. Maier, Enhanced potential of amorphous electrode materials: Case study of RuO_2. *Adv. Mater.* **20**, 501–505 (2008).
62. J. F. Gomez-Garcia, H. Pfeiffer, Structural and CO_2 capture analyses of the $Li_{1+x}FeO_2$ ($0 \leq x \leq 0.3$) system: Effect of different physicochemical conditions. *RSC Adv.* **6**, 112040–112049 (2016).
63. K. B. Yatsimirskii, V. V. Nemoshkalenko, Y. P. Nazarenko, V. G. Aleshin, V. V. Zhilinskaya, N. A. Tomashevsky, Use of X-ray photoelectron and Mössbauer spectroscopies in the study of iron pentacyanide complexes. *J. Electron Spectros. Relat. Phenomena* **10**, 239–245 (1977).
64. H. Wang, M. Matsui, H. Kuwata, H. Sonoki, Y. Matsuda, X. Shang, Y. Takeda, O. Yamamoto, N. Imanishi, A reversible dendrite-free high-areal-capacity lithium metal electrode. *Nat. Commun.* **8**, 15106 (2017).
65. Z. Wang, J. Wang, Z. Li, P. Gong, X. Liu, L. Zhang, J. Ren, H. Wang, S. Yang, Synthesis of fluorinated graphene with tunable degree of fluorination. *Carbon* **50**, 5403–5410 (2012).
66. J.-S. Bridel, S. Grugeon, S. Laruelle, J. Hassoun, P. Reale, B. Scrosati, J.-M. Tarascon, Decomposition of ethylene carbonate on electrodeposited metal thin film anode. *J. Power Sources* **195**, 2036–2043 (2010).
67. W. Li, H. Yao, K. Yan, G. Zheng, Z. Liang, Y.-M. Chiang, Y. Cui, The synergetic effect of lithium polysulfide and lithium nitrate to prevent lithium dendrite growth. *Nat. Commun.* **6**, 7436 (2015).
68. T. Deng, X. Fan, L. Cao, J. Chen, S. Hou, X. Ji, L. Chen, S. Li, X. Zhou, E. Hu, D. Su, X.-Q. Yang, C. Wang, Designing in-situ-formed interphases enables highly reversible cobalt-free $LiNiO_2$ cathode for Li-ion and Li-metal batteries. *Joule* **3**, 2550–2564 (2019).

Acknowledgments

Funding: This work was supported by the National Key R&D Program of China (2016YFB0901600), NSAF (grant no. U1830113), National Natural Science Foundation of China (51772313 and 21975276), and Shanghai Science and Technology Committee (20520710800).

Author contributions: C.Li proposed the idea and designed the project. K.C. performed the experiments with help from Y.Z., J.H., and C.La. M.L. and Z.Y. conducted the first-principles calculations. K.C. and C.Li analyzed the results and wrote the manuscript. **Competing interests:** The authors declare that they have no competing interests. **Data and materials availability:** All data needed to evaluate the conclusions in the paper are present in the paper and/or the Supplementary Materials.

Submitted 23 April 2021
Accepted 10 September 2021
Published 3 November 2021
10.1126/sciadv.abj1491